

Banner appropriate to article type will appear here in typeset article

Noise dissipation mechanisms of an acoustic liner under grazing flow

Francesco Scarano¹, Angelo Paduano¹ and Francesco Avallone¹

¹Department of Mechanical and Aerospace Engineering (DIMEAS), Politecnico di Torino, Corso Duca degli Abruzzi, 24, 10129 Turin, Italy

Corresponding author: Francesco Scarano, francesco.scarano@polito.it

(Received xx; revised xx; accepted xx)

High-fidelity lattice–Boltzmann very-large-eddy simulations are performed to describe the noise dissipation mechanisms in an acoustic liner subjected to grazing turbulent flow at a Mach number of 0.3 and plane acoustic waves. The study examines the effects of sound pressure level (ranging from 130 to 160 dB) and frequency, as well as the direction of acoustic-wave propagation relative to the grazing flow. The considered mechanisms of acoustic energy dissipation are the viscous losses along the internal walls of the orifice and the vortex-shedding. The latter is quantified through Howe’s energy corollary. In the absence of grazing flow, acoustic energy is dissipated almost equally during both inflow and outflow phases, with vortex shedding dominating at high SPL and viscous losses at low SPL. The introduction of a grazing flow alters the flow topology; in particular, the shear layer past the orifice generates a quasi-steady vortex that confines the acoustic-induced flow to the downstream half of the orifice. This topological change modifies the two noise dissipation mechanisms: viscous losses increase at low SPL because the grazing flow pushes the fluid toward the downstream lip of the orifice; vortex shedding becomes phase dependent, dissipating acoustic energy during the inflow phase and generating acoustic energy during the outflow phase. This explains why the net acoustic dissipation decreases in the presence of grazing flow, highlighting the crucial role of near-wall flow topology on liner performances.

Key words:

1. Introduction

Acoustic liners are extensively used in aircraft engines as a passive noise control devices to reduce noise emissions (Motsinger & Kraft 1991a; Winkler *et al.* 2021); they are usually installed in the intake of engines and in the core jet section. The noise source in aircraft engines consists of two main components: a tonal component at the blade-passing frequency (BPF), and a broadband component generated by turbulence impingement, which arises

from the close proximity of the fan to the stator stage (Mallat 1989; Hughes 2011; Casalino *et al.* 2018). Recent development of ultra high bypass ratio engines, characterized by a larger fan diameter compared to traditional high bypass ratio engines, has significantly increased the contribution of fan noise to the overall engine noise.

The simplest acoustic liner is the single-degree-of-freedom (SDOF) one, which comprises a cavity backing a perforated face-sheet (Motsinger & Kraft 1991*b*). In the absence of grazing turbulent flow and high-intensity acoustic waves, a conventional SDOF liner behaves like a Helmholtz resonator. The presence of acoustic waves at a frequency close to that of resonance excites an acoustic-induced flow within the orifice that leads to acoustic dissipation (Tam & Kurbatskii 2000). The resonant frequency of the liner is typically tuned to coincide with the fan's BPF or its harmonics, making SDOF liners particularly suitable for fan noise attenuation. The response of acoustic liners is typically characterized through the impedance, which depends on geometric parameters, sound pressure level (SPL), and flow conditions (Bonomo *et al.* 2023).

The physics of acoustic liners and their dissipation mechanism is well-established when they are exposed solely to acoustic waves (Melling 1973; Tam & Kurbatskii 2000), however a gap persists in the understanding and modelling noise dissipation when the liners operate under real working conditions, i.e. in presence of both acoustic wave and grazing turbulent flow at high Mach numbers and SPL. In the absence of grazing flow, impedance can be directly linked with the absorption coefficient and thus energy dissipation, however this relation does not hold when the liner works in presence of grazing flow and at high SPL (Tam *et al.* 2009).

In absence of grazing flow, energy dissipation in a SDOF liner occurs through viscous losses and via vortex shedding mechanisms. For moderate SPLs, typically below 140 dB, viscous dissipation dominates; it occurs along the internal surfaces of the orifices where laminar boundary layers develop (Tam & Kurbatskii 2000). As the SPL increases and the operating regime transitions into a fully non-linear, the acoustic-induced flow topology is characterized by the emergence of turbulent jets and the shedding of vortices at the orifice entrances (Zhang & Bodony 2012*b*; Tam & Kurbatskii 2000). Here, acoustic energy is transformed into turbulent kinetic energy associated with the rotational motion of vortices, which is ultimately dissipated as heat through viscous processes (Tam & Kurbatskii 2000). According to Tam & Kurbatskii (2000), vortex shedding is amplified near the liner's resonant frequency but remains largely unaffected by the angle of incidence of the acoustic waves. Recent experimental investigations without grazing flow, such as that by Tang *et al.* (2024), have revealed the presence of multi-scale vortex structures driven by acoustic excitation at high SPL.

A detailed understanding of the acoustic response of liners subjected to high-speed turbulent grazing flow and acoustic waves remains incomplete. Under these conditions, liners operate always in the non-linear regime despite the SPL at which they are exposed, and the coupling between flow and acoustics becomes increasingly complex. In particular, the spatial and temporal evolution of the velocity field inside the orifices deviates substantially from the no-flow case (Zhang & Bodony 2016*b*). The interaction between the acoustic-induced flow field and the grazing flow was visualized for the first time by Baumeister & Rice (1975*b*). They identified the presence of a vortex at the upstream side of the orifice neck, leading to a reduction in the effective inflow area. Subsequent computational studies have explored the flow physics inside the orifice in greater detail. Initial investigations focused on simplified configurations without grazing flow (Tam & Kurbatskii 2000), and later extended to include grazing flow conditions.

Shahzad *et al.* (2023) performed direct numerical simulations of a turbulent grazing flow over a lined wall in the absence of acoustic forcing, revealing substantial modifications of

the near-wall flow topology compared to a smooth surface. This was linked with an increase in drag. Fully three-dimensional numerical simulations examining the interaction between acoustic waves and grazing flow over an acoustic liner were performed by Zhang & Bodony (2016*b*). The simulations elucidated the intricate coupling between the flow field and the liner's acoustic response, and how this coupling depends on the state of the incoming boundary layer, laminar or turbulent. Their results showed that the influence of boundary-layer parameters is more pronounced at low SPL. In addition they showed the ejection of vorticity both into the main channel and into the cavity through the orifice, an effect that becomes increasingly pronounced at high SPL, where the influence of the grazing flow weakens. Using micro-particle image velocimetry, Léon *et al.* (2019*a*) investigated how a turbulent grazing flow interacts with a conventional acoustic liner under acoustic excitation. At low SPL, the grazing flow remained essentially unaffected, whereas at higher SPL the acoustic forcing produced mean-flow distortions above the orifice and synthetic-jet-like motions penetrating deeply into the grazing flow. The local state of the turbulent grazing flow, in turn, strongly influences the spatial decay of the SPL along a lined duct. Recent studies by Paduano *et al.* (2025) confirmed that the SPL decays less in the presence of flow over an acoustic liner, suggesting that the underlying noise dissipation mechanisms are locally modified by the turbulent grazing flow.

Despite extensive research efforts, a comprehensive description of the flow dynamics within the liner's orifices and a reliable quantification of acoustic dissipation mechanisms under grazing flow are still lacking. This challenge arises mainly from the difficulty of resolving fine-scale flow features, such as the vorticity field and wall shear stresses on the perforated plate. High-fidelity numerical simulations, complemented by controlled experiments, therefore offer a powerful approach to investigate these phenomena and deepen our understanding of the noise dissipation mechanisms.

In this study, we aim to quantify the contributions of both vortex shedding and viscous dissipation to the overall acoustic energy dissipation. We compare configurations with and without grazing flow and explore the effect of varying SPL, source frequency and acoustic propagation direction, covering both the linear and non-linear regimes. The main research questions guiding this work are:

- How does the presence of grazing flow alter the dissipation of acoustic energy in an acoustic liner?
- How does the change in flow topology inside the orifice influence the dissipation mechanism?
- How do the relative contributions of viscous effects at the orifice walls and vortex shedding vary in the presence of grazing flow, and what is the impact of changing the SPL?

The dissipation by viscous effects at the orifice walls is evaluated following the approach proposed by Tam & Kurbatskii (2000) while the dissipation by vortex shedding is evaluated applying Howe's energy corollary (Howe 1980). The Howe's energy corollary has been previously applied to highlight the mechanisms of generation and absorption of sound in air-jet instruments relying on both numerical (Tabata *et al.* 2021) and experimental (Yoshikawa *et al.* 2012) data.

The analysis are applied to high-fidelity data obtained with lattice-Boltzmann very-large-eddy simulations (LB/VLES) of a fully resolved liner configuration, consisting of a single cavity and a perforated plate with multiple orifices. This approach reduces computational cost while focusing on the dissipation mechanisms of interest. By analyzing a single orifice within one cavity, we can isolate the direct effect of the grazing flow itself from the additional complexities introduced by the development of the flow over a full liner (Paduano *et al.* 2025; Shahzad *et al.* 2025). The liner geometry replicates that used in

previous experimental campaigns conducted in the Grazing Flow Impedance Tube (GFIT) facility at NASA Langley Research Center (Jones *et al.* 2010), as well as in the numerical studies by Zhang & Bodony (2016b).

The paper is organised as follows. Section 2 describes the data reduction methodology, the technique to evaluate the acoustic-induced velocity, and the methods used to quantify dissipation due to vortex shedding and viscous effects. Section 3 outlines the numerical setup, solver details, geometry, and the simulation test matrix. Section 4 focuses on the flow field inside the orifices, examining both the acoustic-induced velocity distribution inside the orifice and the shear layer development at the orifice mouth. Finally, Sections 5 and 6 present the analysis of the dissipation mechanisms, and Section 7 concludes the paper.

2. Data reduction methodology

2.1. Dissipation by viscous effects at the orifice walls

Following the approach reported by Tam & Kurbatskii (2000), the rate of energy dissipation due to viscosity can be calculated from the instantaneous velocity field. The dissipation rate $D(t)$ can be calculated by integrating the stress tensor over the internal surface of the orifice resonator where a boundary layer-like flow is formed

$$D(t) = \iint_{\text{orifice walls}} \sigma_{ij}(x, y, t) \frac{\partial u_i}{\partial x_j} dx dy \quad (2.1)$$

where σ_{ij} is the general expression of the stress tensor

$$\sigma_{ij}(x, y, t) = \mu \left(\frac{\partial u_i}{\partial x_j} + \frac{\partial u_j}{\partial x_i} \right). \quad (2.2)$$

The dissipation rate can be phase averaged in order to evidence the variation over one period of forcing. In the following it is described as a function of the phase of the sinusoidal acoustic forcing, $D(\phi)$.

The energy dissipated by viscous effects per unit time, E_{viscous} , can be obtained by integrating $D(\phi)$ over the period of oscillation, T ,

$$E_{\text{viscous}} = \frac{1}{T} \int_0^T D(\phi) d\phi. \quad (2.3)$$

2.2. Dissipation by vortex shedding: Howe's energy corollary

The conversion of acoustic energy into vortex shedding can be quantified using Howe's energy corollary (Howe 1975, 1980, 1984). According to this formulation, the power density transferred from the acoustic field to the vortical field is given by:

$$\Pi_g(x, y, t) = \rho_0(\omega \times \mathbf{u}') \cdot \mathbf{u}_{\text{ac}}, \quad (2.4)$$

where ρ_0 is the mean fluid density, ω is the vorticity, and $\mathbf{u}' = \mathbf{U} + \mathbf{u}_{\text{aero}} + \mathbf{u}_{\text{ac}}$ represents the total velocity field, composed of the aerodynamic fluctuating component \mathbf{u}_{aero} and the acoustic component \mathbf{u}_{ac} plus the mean flow, \mathbf{U} .

The acoustic energy conversion rate into vorticity within the domain composed by the orifice and the portions of the channel and the cavity, enclosing the vortical structures, is then expressed as:

$$\Pi(t) = \iint_{\text{orifice area}} \Pi_g(x, y, t) dx dy. \quad (2.5)$$

A positive value of $\Pi_g(x, y, t)$ or $\Pi(t)$ indicates the absorption of acoustic energy by the vortical field, while a negative value corresponds to acoustic energy generation by the formation of vortical field. As for the viscous dissipation rate, the acoustic energy conversion rate into vorticity can be expressed as a function of the phase, by phase averaging the time-series.

The net energy transferred between the acoustic and the vortical field per unit time over a period of oscillation T is given by:

$$E_{\text{shedding}} = \frac{1}{T} \int_T \Pi(\phi) d\phi. \quad (2.6)$$

2.3. Acoustic-induced velocity estimation

To evaluate Howe's energy corollary, it is necessary to isolate the acoustic-induced velocity field inside the orifices from the perturbations caused by the external turbulent grazing flow. In this work, the acoustic-induced velocity is obtained using spectral proper orthogonal decomposition (SPOD) (Schmidt & Colonius 2020), following the approach of Scarano *et al.* (2025).

SPOD yields an orthogonal modal basis from statistically stationary data, in which most of the energetic, temporally coherent fluctuations are concentrated in the leading modes. As highlighted by Schmidt & Colonius (2020), SPOD combines produces spatial structures that are both energy-optimal and temporally correlated. The MATLAB routines of Towne *et al.* (2018) are used here to perform the decomposition and velocity reconstruction.

The reduced-order model (ROM) for reconstruction is built from the leading SPOD mode within the frequency band centred at the forcing frequency. Prior to reconstruction, a band-pass filter is applied to the SPOD coefficients.

It is important to emphasize that the acoustic-induced velocity reconstructed with SPOD represents the coherent contribution extracted through modal decomposition. This coherent fraction should not be directly associated with the irrotational component of the velocity field, as in a Helmholtz decomposition (Schoder *et al.* 2020; Unnikrishnan & Gaitonde 2020). Instead, the reconstruction based on the source frequency isolates the portion of the flow that best captures the coherent acoustic-induced velocity relevant to the present analysis.

3. Numerical setup and database description

3.1. Numerical solver

The commercial software 3DS Simulia PowerFLOW 6-2019R4 is used to compute the transient flow field. The solver has already been validated for canonical honeycomb liner configurations, both in the absence of flow (Mann *et al.* 2013; Hazir & Casalino 2017) and with grazing flow (Manjunath *et al.* 2018; Avallone *et al.* 2019). The same solver has also been used to simulate the effect of a SDOF liner installed on the nacelle of the NASA Source Diagnostic Test engine configuration (Casalino *et al.* 2017), and the predicted sound attenuation has recently been confirmed by another simulation carried out by using a different high-fidelity flow solver (Shur *et al.* 2021).

PowerFLOW flow simulation technology is based on a LB method with collision relaxation time and distribution function dynamically calibrated to the time scales of slow turbulent structures modelled through a turbulence transport model. Some of the key properties of the model are described in the following paragraphs with reference to literature.

The LB scheme is based on an expansion of the distribution function $f(\mathbf{x}, \xi, t)$, say the probability density of finding particles at location \mathbf{x} , advected at velocity ξ at time t , solution of the Boltzmann equation, in a series of Hermite polynomials (Shan *et al.* 2006). These constitute an orthogonal basis, which is particularly suited to describe a flow in the kinetic space. Indeed, the first four coefficients, from 0th to 3rd order, of the expansion of the Maxwellian distribution function $f^{(0)}$ at equilibrium are algebraically related to the moments of macroscopic flow, say mass, momentum, energy/momentum fluxes, and heat fluxes. An interesting property of a Hermite expansion is that the series can be truncated at a given order without altering the low-order coefficients; therefore an expansion of f truncated at the order $N > 3$ provides a unique representation of the macroscopic hydrodynamic status of a fluid.

A key component of PowerFLOW LB scheme is the usage of a regularized collision operator Ω_i in the non-dimensional lattice Boltzmann equation

$$f_i(\mathbf{x} + \xi_i, t + 1) = f_i(\mathbf{x}, t) + \Omega_i \quad (3.1)$$

projected along the discrete particle velocity ξ_i . Following Zhang *et al.* (2006), the LB equation can be equivalently written as

$$f_i(\mathbf{x} + \xi_i, t + 1) = f_i^{(0)}(\mathbf{x}, t) + f_i^{(1)}(\mathbf{x}, t) + \Omega_i \quad (3.2)$$

where $f_i^{(1)}$ is the perturbation. In conditions that are not very far from equilibrium, the collision operator is linearly related to the perturbation through coefficients that are negatively/inversely proportional to relaxation time τ_{ij} of the collision process along the discrete velocity direction i due to chaotic motion along the direction j , say

$$f_i(\mathbf{x} + \xi_i, t + 1) = f_i^{(0)}(\mathbf{x}, t) + \sum_j (\delta_{ij} - 1/\tau_{ij}) f_i^{(1)}(\mathbf{x}, t). \quad (3.3)$$

If the perturbation is expanded in Hermite series, this starts by the second order term and can be truncated at the third order term to recover the macroscopic fluid status. The resulting regularized collision operator will therefore include only terms proportional to the second order Hermite polynomials, accounting for energy and momentum fluxes, and third order terms polynomials, accounting for heat fluxes. Finally, following Chen *et al.* (2014), applying Galilean invariance to the collision operator results in a two-term regularized form, in which the two terms account for energy/momentum fluxes and heat fluxes, respectively, with corresponding relaxation times related to the macroscopic fluid viscosity and thermal conductivity.

Another important component of the present flow simulation methodology is related to turbulence modeling, which is key to tackle high Reynolds number flows. The way turbulence is accounted for in PowerFLOW is by modifying the relaxation time in the collision operator by considering the time scales related to the turbulent motion and to the strain rate and rotation of the resolved flow field. Moreover, the amount of turbulent kinetic energy is used to define the equilibrium state of the gas. Such a procedure is based on the paradigm of a kinetic theory applied to a “gas of eddies” and it can be interpreted as an expanded analogy between the chaotic motion of particles (and the internal energy) and the chaotic motion of eddies (and the turbulent kinetic energy), which is indeed the essence of the Boussinesq analogy. As discussed by Chen *et al.* (2004), the expansion of the kinetic theory from particles to eddies leads to the fundamental observation that the Reynolds stresses, which are a consequence of the chaotic turbulent motion, have a non-linear structure and are better suited to represent turbulence in a state far from equilibrium, as in the presence of distortion, shear, and rotation. In other words, although the

relaxation time is computed using the two-equation $k-\epsilon$ Re-Normalization Group (RNG) model in PowerFLOW (Yakhot *et al.* 1992; Teixeira 1998), this model is not employed to compute an equivalent eddy viscosity, as in traditional Reynolds-Averaged Navier–Stokes (RANS) formulations. Instead, it is used to dynamically recalibrate the Boltzmann model to the characteristic time scales of turbulent flow motion. Hence, no Reynolds stresses are explicitly added to the governing equations, and they are an implicit consequence of the chaotic exchange of momentum driven by the turbulent flow with characteristic times smaller than the slowly-varying turbulent flow. The underlying concept of a dynamic gas system continuously driven towards equilibrium as a consequence of an intimate coupling between the LB kinetic model and the turbulence transport model is the essence of the LB/VLES hybrid approach.

The LB/VLES equations are solved on a Cartesian mesh which is automatically generated for any complex shape of the boundary conditions. Variable resolution (VR) regions can be defined in the flow domain to locally refine the grid size by successive factors of 2. By construction, in a time step particles are advected exactly from one point to the other points of the lattice stencils. Therefore, the local time step varies by a factor 2 in adjacent VRs. Bounce-back boundary condition for no-slip walls and the specular reflection for frictionless walls are ensured thanks to a generalized volumetric formulation for the intersection of arbitrary-oriented surface elements and the volume elements (Chen & Doolen 1998). Finally, a wall-model accounting for pressure gradients is used to boundary layer behaviours at high Reynolds numbers (Teixeira 1998).

3.2. Computational domain

The acoustic liner geometry is similar as the one experimentally investigated by Jones *et al.* (2004) in the GFIT facility at NASA Langley Research Center at several free-stream Mach numbers and computationally investigated by Zhang & Bodony (2016b) at free-stream Mach number equal to 0.5. The liner is shown in Figure 1. A rigid face sheet of thickness $\tau = 0.64$ mm is perforated with cylindrical holes of diameter $d = 0.99$ mm, which corresponds to a length-to-diameter ratio of 0.65. A single honeycomb cavity with 7 orifices is studied, thus resulting in a porosity of $\sigma = 6.4\%$ very close to the reference study ($\sigma = 8.7\%$). While in the experimental study the orifices are randomly located such that they can overlap neighbouring cavities, in this study, six orifices are placed at the center of each of the six equilateral triangles that form the hexagon and one at its centre. The cell depth is $d_c = 38.10$ mm and the distance between the two opposite corners of the cell is $l_c = 9.5$ mm. A rigid back plate closes the cell from below and the cell walls are rigid, so that, in the experiments, neighbouring cells cannot communicate.

The acoustic liner is grazed by a turbulent flow with free stream Mach number equal to $M = 0.3$. The liner is placed along the top wall of a duct that has a rectangular cross section with height, h_c , equal to 63.5 mm, as in the GFIT facility, while the width is restricted to 12 mm to reduce the computational cost. Transition to turbulence is forced using a zig-zag strip at 1750 mm upstream of the liner. The zig-zag strip is 1 mm thick, it has length and wavelength equal to 10 mm and angle of 60° . The location of the zig-zag trip has been selected such to replicate the time-average turbulent boundary layer profile measured in the GFIT (Jones *et al.* 2010). The velocity profile upstream of the liner has a displacement thickness δ^* equal to 3×10^{-2} m and momentum thickness δ^\dagger equal to 1.96×10^{-3} m. These parameters are very close to the ones measured experimentally by Jones *et al.* (2010). The resulting in a Reynolds number based on the momentum thickness Re_{δ^\dagger} equal to 14000.

The streamwise coordinate, x , is aligned with the grazing flow direction (from left to right in the figures), the spanwise coordinate is z , and the wall-normal coordinate is y . The origin of y is located on the outer surface of the perforated plate exposed to the flow,

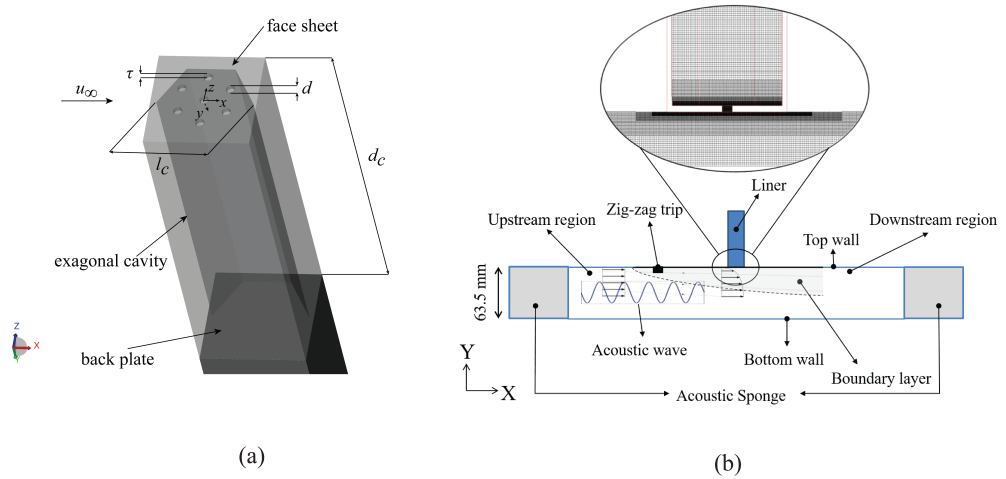


Figure 1. (a) Schematic of the cavity with representation of the coordinate reference system. The y axis is oriented towards the inside of the cavity. (b) Schematic of the computational setup with the grid in a plane crossing the central orifice.

with positive y directed into the cavity. The nomenclature for the velocity components is the following: u', v', w' are the instantaneous velocity components, U, V, W stand for the time-average values, and u, v, w are the fluctuating components according to the Reynolds decomposition.

Periodic boundary conditions are applied on the side walls, no-slip boundary condition on the top wall and slip boundary condition on the bottom wall. At the inlet, free stream velocity corresponding to the free-stream Mach number is assigned while pressure boundary condition is set at the outlet. Additional acoustic sponge regions, where viscosity is increased, are placed at the inlet and outlet of the computational domain to dampen the reflection of acoustic waves.

Computations are carried out with a two-step approach: first the turbulent boundary layer convecting in the duct is computed and temporal convergence is verified; an instantaneous flow field is saved and is modified by superimposing a plane acoustic wave, with given frequency and amplitude, using the *Opty@B* toolkit. The modified flow field is used to seed the high-fidelity numerical simulations with acoustic waves. This approach has the advantage to reduce the computational cost when there is the need of studying many different configurations as in the present case.

The analysis is conducted on a two-dimensional streamwise plane extracted from the numerical simulation, encompassing a region that includes the central orifice of the cavity, together with a portion of the cavity and the channel above and below it. The domain considered extends over approximately 3×4.5 orifice diameters. The limited streamwise extent of the computational domain, together with the periodic spanwise boundary condition, ensures that three-dimensional effects remain negligible compared to the grazing flow, thus making the 2D field analysis representative of the orifice dissipation mechanisms. A schematic of the computational setup is reported in Figure 1, where an example of the computational grid close to cavity is shown. In the computations, 10 resolution regions are used; the smallest voxels are used to discretize the computational domain close and within the orifices. The maximum resolution adopted in this paper is $40 \text{ voxels/mm} \approx 40 \text{ voxels}/d$. This is similar to the value suggested by Manjunath *et al.* (2018) in absence of acoustic waves of $\approx 42 \text{ voxels}/d$.

case	SPL [dB]	f [Hz]	M	ac. prop. direction
Validation against GFIT Jones <i>et al.</i> (2004)	-	-	0.3	-
Validation against GFIT Jones <i>et al.</i> (2004)	130	1800, 2200, 3000	0.0	x^+
Effect of SPL	130,140,150,160	2200	0; 0.3	x^+
Effect of source frequency	150	1800, 2200, 3000	0; 0.3	x^+
Effect of flow direction	150	2200	0.3	$x^+; x^-$

Table 1. List of the simulations carried out

Surface data for the estimation of the impedance is sampled at a frequency of 20 kHz. The flow field is on the other hand sampled such to have 720 point per wavelength. For each configurations, acoustic waves with 10 acoustic periods are considered based on the findings from previous studies from the authors (Manjunath *et al.* 2018; Avallone *et al.* 2019) and DNS results by Zhang & Bodony (2016b). Data are sampled after convergence of the unsteady field, which is in general obtained after no more than 2 acoustic periods.

3.3. Test cases and simulation strategy

The test matrix is summarized in Table 1. Five sets of simulations are considered.

The first test case considers the simulation with grazing flow only and is used to validate the incoming flow conditions against the results reported by Jones *et al.* (2004). The second test case corresponds to the condition without grazing flow, in which the SPL, expressed in decibels using a reference pressure of 20×10^{-6} Pa, is fixed at 130 dB while the source frequency is varied. This configuration serves as a validation and allows direct comparison of the impedance results with those obtained in the GFIT facility. The grid convergence assessment, along with the validation of the incoming flow conditions and the impedance in the absence of grazing flow, are presented in Appendix A.

The third test case constitutes the core of the present analysis. The frequency of the grazing acoustic wave is fixed at 2200 Hz, which is higher than the resonant frequency in the absence of flow (which is approximately equal to 1600 Hz, calculated using the method proposed by Panton & Miller (1975)) but closer to the resonant frequency in presence of grazing flow. Both with and without grazing turbulent flow at $M = 0.3$, the SPL is varied systematically. This enables the investigation of dissipation mechanisms across linear and nonlinear regimes, and how these are modified by the presence of grazing flow.

The fourth test case explores the effect of changing the source frequency at a fixed SPL of 150 dB, for both configurations with and without grazing flow. This dataset provides insight into the frequency dependence of the dissipation mechanisms.

Finally, the last test case addresses the role of acoustic propagation direction relative to the grazing flow. In the x^+ configuration, the acoustic waves propagate in the same direction as the grazing flow, whereas in the x^- configuration they propagate in the opposite direction. The latter scenario is particularly relevant, as it closely resembles the operating condition of acoustic liners installed in engine nacelles, where the grazing flow enters from the upstream side while the dominant acoustic waves are generated downstream by the fan and travel in the upstream direction.

4. Flow field within the orifice

4.1. Acoustic-induced velocity profiles within the orifice

To characterise the interaction between the acoustic waves and the grazing flow, we focus on the vertical acoustic-induced velocity component, v_{ac} , which is directly linked to the conversion and dissipation of acoustic energy (Tam & Kurbatskii 2000). The impinging acoustic plane wave generates a periodic exchange of mass through the orifice of the liner (Zhang & Bodony 2016a). The phase of the acoustic oscillation is indicated by ϕ . The inflow phase ($\phi = \pi/2$) corresponds to the instant of maximum mass flux entering the cavity, while the outflow phase ($\phi = 3\pi/2$) denotes the instant of maximum mass flux exiting the cavity.

Figure 2 and figure 3 show the contours of the acoustic-induced velocity during the inflow and outflow phases, for the cases without and with grazing flow, respectively. The effect of the SPL is reported in each figure. The reconstructed velocity field is normalized with respect to the velocity of the lumped element model of the Helmholtz resonator (Morse & Ingard 1968):

$$v_{ac}^* = \frac{p'}{\rho\omega(\tau + 0.8d)} \frac{1}{\sqrt{[(\omega_H/\omega)^2 - 1]^2 + (\omega_H/\omega Q)^2}}, \quad (4.1)$$

where p' is the pressure fluctuation amplitude, ω and ω_H are the forcing and resonant frequencies, Q is the quality factor (taken as 10), ρ is the density, and d and τ are the diameter and thickness of the orifice, respectively. This expression gives theoretical peak velocities of approximately 3.6, 9.5, 30.2, and 67.6 m/s for the four tested SPLs.

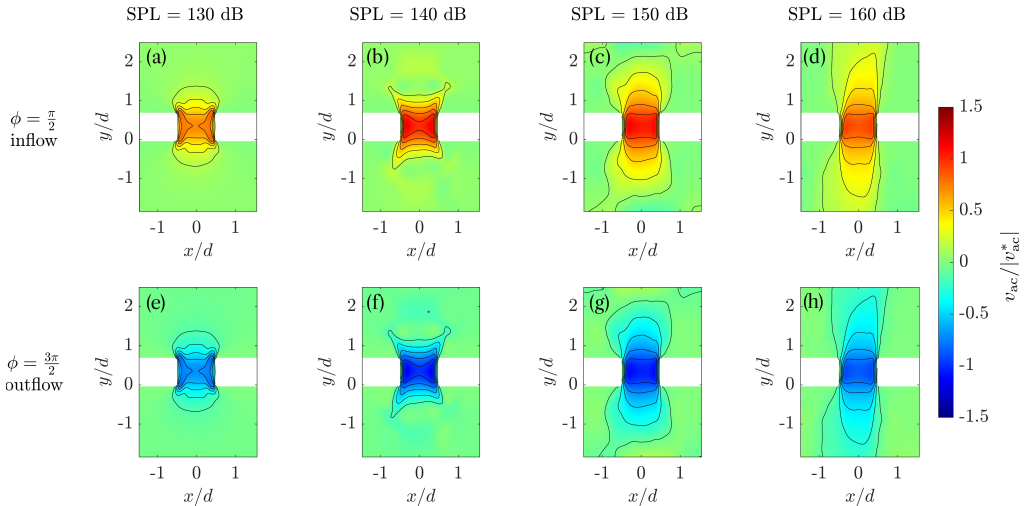


Figure 2. Contour of the wall-normal acoustic-induced velocity at the inflow ($\phi = \pi/2$) and outflow ($\phi = 3\pi/2$) phases, effect of the SPL (left to right column), no flow condition.

Although this formula does not account for grazing flow, it has been employed in previous studies of acoustic liners (Zhang & Bodony 2016b, 2012a; Scarano *et al.* 2025). Among possible normalizations (free-stream velocity, friction velocity, speed of sound), the theoretical acoustic-induced velocity is the most suitable, as it also allows verification of the order of magnitude of the results. In cases without grazing flow, the normalized acoustic-induced velocity should be of order one (Léon *et al.* 2019b).

For the no-flow case, the acoustic-induced velocity shows high amplitude on the entire orifice extent, and the inflow and outflow phases are almost perfectly symmetric. As the SPL increases, the distribution of the acoustic-induced velocity becomes broader, extending deeper into the cavity ($y/d > 0.6$) during the inflow phase and farther into the channel ($y/d < 0$) during the outflow phase. For instance, at SPL = 130 dB (figure 2 (a-e)), the velocity field exhibits high velocity amplitude only in the vicinity of the orifice, while it attenuates rapidly within approximately one diameter in the wall-normal direction; at higher SPL, the region of influence extends farther from the wall. A boundary layer region at the orifice side walls is also visible which is consistent to what reported by Zhang & Bodony (2012a).

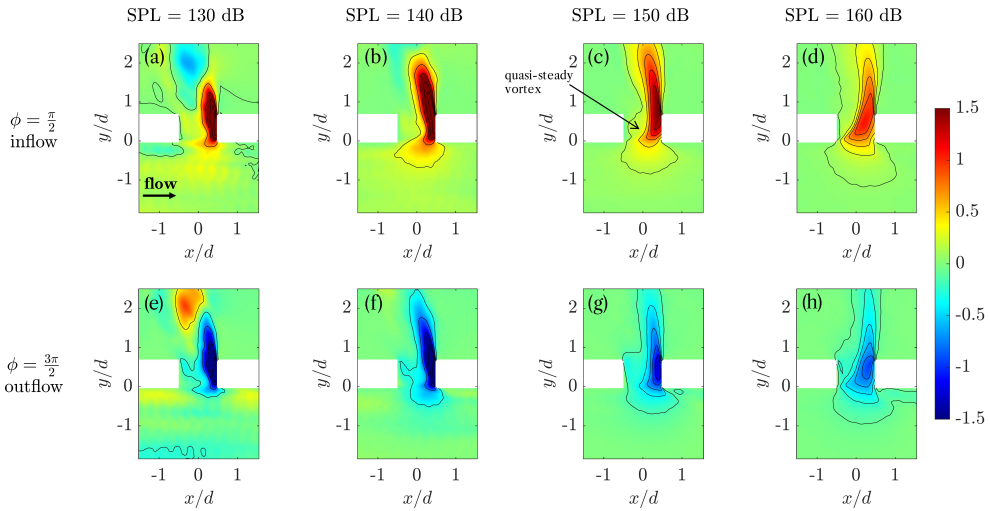


Figure 3. Contour of the wall-normal acoustic-induced velocity at the inflow ($\phi = \pi/2$) and outflow ($\phi = 3\pi/2$) phases, effect of the SPL (left to right column), $M = 0.3$.

When grazing flow is introduced, the flow topology of the acoustic-induced velocity changes markedly, in agreement with Zhang & Bodony (2016b) and Paduano *et al.* (2025). The acoustic-induced velocity becomes concentrated in the downstream half of the orifice, displaying a jetting-like pattern during the inflow and outflow phases, while the upstream half is occupied by a quasi-steady vortex resulting from the vena contracta effect. The formation of this quasi-steady vortex reduces the effective porosity of the orifice, leading to increased flow blockage and a corresponding shift of the liner’s resonant frequency toward higher values. This aspect will be further discussed in the section dedicated to the frequency-dependent analysis of the dissipation mechanisms. In addition, the increased blockage induced by the grazing flow, and the consequent reduction in effective porosity, is presumed to contribute to the rise in acoustic resistance, as discussed in Appendix A, where the impedance calculations are presented.

As the SPL increases (figure 3 (c-g and d-h)), the extent of this quasi-steady vortex diminishes, and peaks of acoustic-induced velocity are localized farther into the cavity. However, unlike the no-flow case, the inflow and outflow phases are largely asymmetric due to the shear imposed by the grazing flow, which acts as a barrier especially in the outflow phase. At high SPL, the amplitude of the pressure fluctuations generates a vertical velocity comparable to the grazing flow velocity, affecting the near-wall region more strongly in the outflow phase (figure 3 (h)).

The velocity profiles taken at mid-height of the orifice are shown in figure 4 for the grazing flow (continuous lines) and the no-flow (dashed lines) cases at $y/\tau = 0.5$ at four phases. In the presence of flow, the velocity does not vanish at the walls because of the finite extent of the exported computational domain in PowerFLOW and of the wall model. Nevertheless, the near-wall velocity gradients, computed through the wall model applied at the orifice walls, are directly provided by the solver and are used for the evaluation of viscous dissipation.

In the absence of flow, the velocity profiles are nearly symmetric across the orifice, with small streamwise asymmetries arising from the grazing nature of the acoustic wave. The peak acoustic-induced velocity matches the theoretical value closely across all SPLs. Remarkably, in presence of grazing flow, at low SPL (figure 4 (a,b)) the peak of the acoustic-induced velocity is about twice that of the no-flow case and exceeds the theoretical prediction by a factor two. This suggests that the grazing flow energy adds to the acoustic energy, pushing flow into the downstream half of the orifice at velocities higher than the ones obtained in absence of grazing flow. This means that the flow contribution dominates at low SPL; this scenario is consistent with the observed broadband amplification of SPL by the turbulent grazing flow found by Roncen (2025) and a transfer of energy from the broad frequencies associated with the turbulence field to the tonal frequency of the acoustic field. When SPL exceeds 140 dB, the theoretical value of acoustic-induced velocity is recovered, indicating that the acoustic forcing overcomes the effect of the grazing flow.

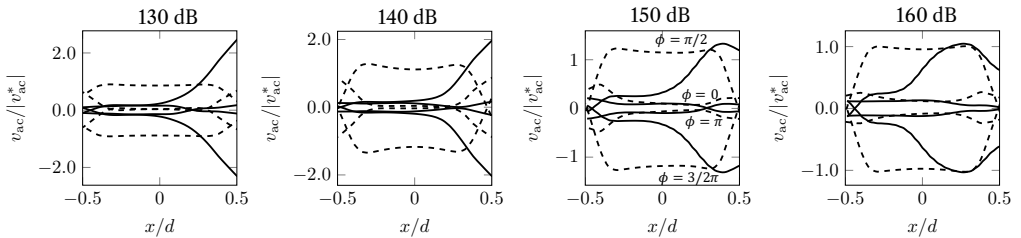


Figure 4. Spatial distribution along the diameter of the non-dimensional acoustic-induced vertical velocity v_{ac} as a function of the SPL at half orifice thickness. Various phases are reported, dashed line is the no flow case and solid line is $M = 0.3$ case.

With grazing flow, the maximum and minimum of the v_{ac} profiles are consistently located in the downstream half of the orifice, around $x/d \approx 0.8$, due to the quasi-steady vortex which acts as a barrier to the acoustic waves. This spatial asymmetry could be responsible for the increased acoustic resistance by effectively reducing the orifice cross-section. As the SPL increases, the location of the maximum v_{ac} shifts toward the orifice centre and the distribution along the orifice diameter becomes more symmetric, indicating an increased acoustic-induced mass flow.

Overall, the effect of the grazing flow is to concentrate the acoustic-induced velocity in the downstream corner, and to increase the peak value relative to the no-flow case at low SPL. The effective porosity, linked to the area available for the acoustic-induced flow, increases with SPL as the acoustic forcing becomes dominant, reducing the blockage effect of the quasi-steady vortex.

4.2. Shear layer at the orifice mouth

The development of the shear layer over the orifice of the acoustic liner, induced by the near-wall mean velocity gradient imposed by the grazing flow, is examined through the contour of the friction velocity shown in figure 5. The grazing flow acts as a barrier that

limits the penetration of the acoustic-induced flow into the orifice, while variations in the SPL modify the shear layer above it. The friction velocity is defined as

$$U_\tau = \sqrt{\nu \frac{dU}{dy}},$$

where U is the mean streamwise velocity, computed over a time window encompassing more than ten acoustic cycles, and ν the kinematic viscosity. Only the grazing flow configuration is shown, since U_τ is meaningful exclusively in the presence of a mean flow over the orifice.

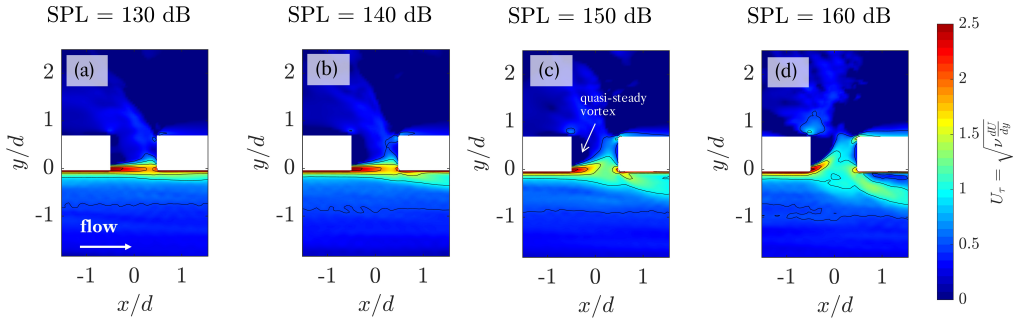


Figure 5. Contour of the friction velocity [m/s] to represent the shear layer forming at the mouth of the orifice in the presence of grazing flow at $M = 0.3$, effect of the SPL.

At low SPL (figure 5 (a-b)), the shear layer blocks the acoustic-induced velocity from entering the orifice over the majority of the diameter extension. The friction velocity remains high across most of the orifice diameter, except for a small downstream region where it slightly decreases. This confirms that the grazing flow constrains the acoustic-driven inflow, localizing it only near the downstream corner. The majority of the orifice is occupied by a quasi-steady vortex (Baumeister & Rice 1975a); at SPL = 130 dB, this vortex extends over nearly the entire orifice diameter (figure 5 (a)). This flow pattern is consistent with the contour of the acoustic-induced velocity reported in figure 3 (a).

As the SPL increases, the size of the quasi-steady vortex progressively diminishes. At 140 dB (figure 5 (b)), approximately half of the cavity depth shows a reduction in friction velocity, suggesting that the acoustic excitation partially overcomes the shear-layer blockage. At 150 dB (figure 5 (c)), the strong shear region is further reduced: a significant portion of the orifice cross-section exhibits lower U_τ . The larger extent and magnitude of the acoustic-induced velocity during the inflow and outflow (see figure 3 (c)) leads to a disruption of the shear layer. This in turn affects the near-wall flow topology inside the channel. This scenario, in fact, reveals wake-like features downstream of the orifice, indicating that the combination of the orifice geometry and the high acoustic-induced flow modifies the near-wall flow development downstream of the orifice.

At 160 dB the disruptive effect of the acoustic-induced flow on the shear layer over the orifice is further enhanced (figure 5 (d)). The high friction velocity region extension is reduced and the shear bends into the orifice. The size of the quasi-steady vortex is consequently reduced, it occupies only the upstream half of the orifice. This results in a stronger and more extended acoustic-induced flow in and out of the cavity compared to lower SPLs. Moreover, the wake-like behaviour downstream of the orifice becomes stronger, suggesting the onset of local flow separation downstream of the orifice.

Similar observations on U_τ were reported by Léon *et al.* (2019b), who documented vortex shedding and the ejection of vortices from the cavity into the grazing flow. Their study proposed that when the ratio between the peak acoustic-induced velocity and the local U_τ exceeds approximately two, the effect of the acoustic forcing becomes sufficiently strong to generate vortices ejected in the grazing flow; otherwise, the influence on the grazing flow remains limited. However, it should be noted that their analysis was conducted outside the orifice, close to the wall, using micro-PIV measurements, whereas the present numerical results allow for an exploration of the flow topology within the orifice. In the present study, the peak acoustic-induced velocity is estimated as 7.6, 19, 36.2 and 67.2 m/s for SPL levels of 130, 140, 150 and 160 dB, respectively, while the friction velocity U_τ of the grazing flow is approximately 4.1 m/s. The resulting ratios are thus roughly 1.8, 4.6, 8.8 and 16.4. Excluding the case at 130 dB the values exceed the threshold suggested by Léon *et al.* (2019b), indicating a significant influence of the acoustic forcing on the flow structure inside and around the orifice, particularly at higher SPL. The quantitative impact of the observed changes in flow topology and the development of the shear layer under grazing flow on the noise absorption mechanism is assessed in the following section through a detailed analysis of acoustic dissipation.

5. Acoustic dissipation analysis

5.1. Acoustic dissipation by vortex shedding

The contours of the power density transferred from the acoustic field to the vortical field, $\Pi_g(\phi)$, at different SPL levels are shown in figure 6 and figure 7 for the no-flow condition and for grazing flow at $M = 0.3$, respectively. In these plots, regions contributing to acoustic dissipation by vortex shedding appear in red, while regions associated with acoustic generation are shown in blue. Two characteristic phases are highlighted: the inflow phase ($\phi = \pi/2$) and the outflow phase ($\phi = 3\pi/2$).

In the absence of grazing flow (figure 6), at the lower SPL levels, 130 and 140 dB, the power density transferred from the acoustic field to the vortical field is negligible. This observation is consistent with the observations reported by Tam & Kurbatskii (2000) who showed that for SPL below 150 dB the contribution of vortex shedding to the overall dissipation is minimal. As the SPL increases to 150 dB, positive regions of Π_g associated with vortical structures appear at the orifice mouth during both the inflow and outflow phases. At 160 dB, these patterns become clearly visible: vortices form at the orifice mouth and roll up either inside the cavity (inflow) or into the channel region (outflow). These regions, identifiable both in the inflow and in the outflow, contribute to the rate of acoustic energy dissipation by vortex shedding.

When the grazing flow is introduced, the dissipation mechanism changes significantly. Even at low SPL, the magnitude of $\Pi_g(\phi)$ increases compared to the no-flow case, suggesting that turbulence structures and shear-layer vortices enhance the transfer of acoustic energy into vorticity. The contours of Π_g follow the topology dictated by the friction and the acoustic-induced velocity. The regions with non-negligible values of Π_g are localized in fact in the downstream half of the orifice due to the presence of the quasi-steady vortex in the upstream half. The magnitude of Π_g and the portion of the domain, which contributes to the conversion of acoustic energy, increase with SPL. During the inflow phase, the positive contribution of Π_g is linked with a vortex generated at the upstream lip of the orifice. This vortex rolls up and penetrates farther into the cavity as SPL increases. In contrast, during the outflow, Π_g assumes negative values. The orifice behaves locally as a noise source: the outward acoustic jet perturbs the grazing flow, leading to the

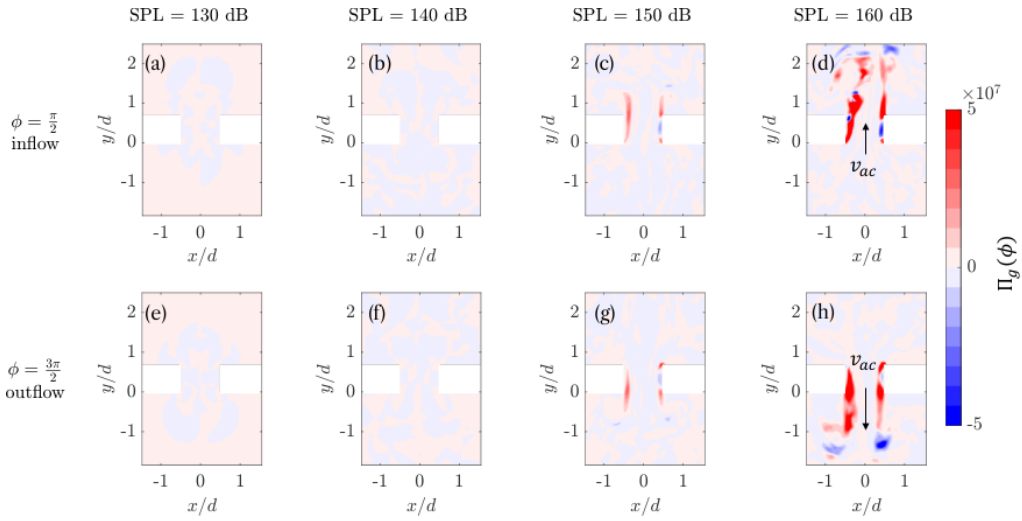


Figure 6. Contour of the power density Π_g [$\text{Kg}/(\text{m}\cdot\text{s}^2)$] transferred from the acoustic field to the vortical field during the inflow and outflow phases when varying the SPL. No-flow, forcing frequency equal to 2200 Hz.

formation of vortical structures that are convected downstream. At 160 dB the negative contribution extends in the channel following a wake-like pattern downstream of the orifice.

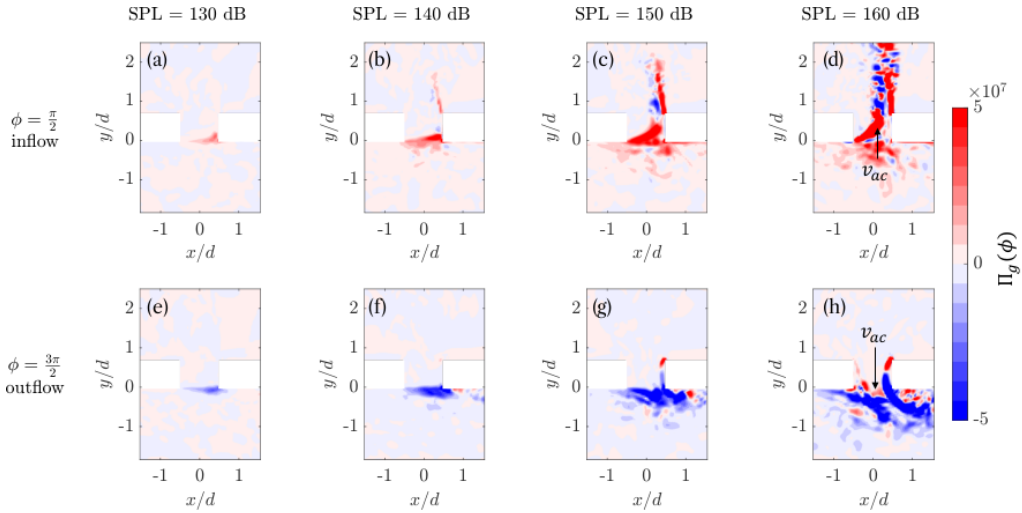


Figure 7. Contour of the power density Π_g [$\text{Kg}/(\text{m}\cdot\text{s}^2)$] transferred from the acoustic field to the vortical field during the inflow and outflow phases when varying the SPL. $M = 0.3$, forcing frequency equal to 2200 Hz.

The evolution of the rate of acoustic dissipation integrated over the domain against the phase, $\Pi(\phi)$, is presented in figure 8. In the absence of grazing flow (figure 8 (a)), $\Pi(\phi)$ exhibits two distinct positive peaks in the inflow and outflow phases. This indicates that dissipation by vortex shedding occurs in both phases. These peaks become more pronounced when increasing the SPL, whereas at 130 and 140 dB the dissipation rate is negligible, as expected (Tam & Kurbatskii 2000).

The evolution of $\Pi(\phi)$ in the presence of grazing flow is shown in figure 8(b). Similarly to the no-flow case, the amplitude of the dissipation rate increases with SPL. However, at

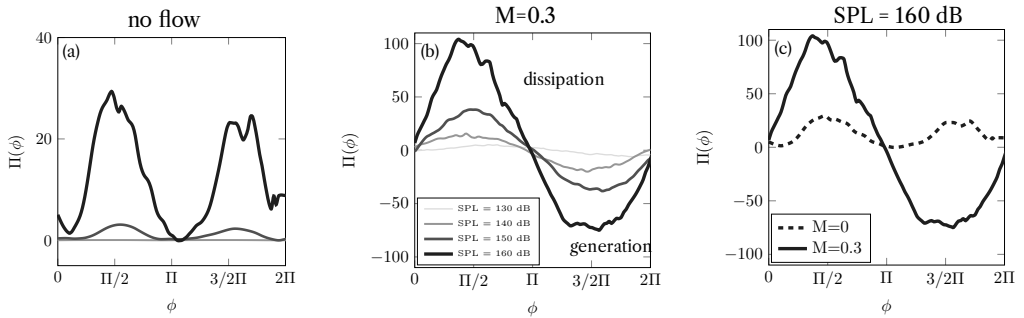


Figure 8. Phase averaged acoustic energy dissipation rate by vortex shedding as a function of the phase, $\Pi(\phi)$ [W/(m-s)], (a) for the no-flow case and (b) for the $M = 0.3$ case when varying the SPL (darker and thicker lines indicate higher SPL); (c) comparison of no-flow and $M = 0.3$ case at 160 dB.

all SPL levels, the system exhibits a positive dissipation rate during the inflow phase and a negative one during the outflow phase. As a result, the net acoustic dissipation over a full cycle is lower than in the no-flow condition, despite the higher instantaneous values of $\Pi(\phi)$ observed during the inflow phase with grazing flow. This is clearly illustrated in figure 8(c) for SPL = 160 dB, where the peak dissipation with grazing flow exceeds that of the no-flow case, yet the overall effect over a complete acoustic cycle is reduced due to the generation of acoustic energy during the outflow phase. This aspect will be further quantified in the acoustic energy budget presented in §5.3.

These findings suggest that, in presence of grazing flow, the outflow phase contributes to the generation of acoustic energy because of the interaction of the outflow of acoustic-induced velocity with the turbulent grazing flow. The system thus exhibits a behaviour analogous to that of a jet in cross-flow, a configuration known to enhance noise radiation (Camelier & Karamcheti 1976; Stimpert & Fogg 1973). Consequently, the overall amount of acoustic energy dissipated by the liner through vortex shedding decreases in the presence of grazing flow compared with the no-flow condition.

5.2. Acoustic dissipation by viscous effects at the mouth of the orifice

Contours of the shear stress tensor, which contributes to the viscous dissipation, are shown in figure 9 for the no-flow condition. The contour scale changes for each subplot with SPL due to the increase in acoustic-induced velocity inside the orifice, which results in larger velocity gradients. In the no-flow case, we observe that both the contour levels and the thickness of the boundary layer developing in the internal walls of the orifice increase with SPL. This trend reflects the rise in the amplitude of the acoustic-induced velocity.

At all SPL levels, the viscous dissipation regions are nearly symmetric across the orifice, with slight asymmetries becoming more pronounced as SPL increases, attributed to the grazing nature of the incident acoustic wave. Figure 10 shows the dissipation rate as a function of phase, separated into contributions from the left and right sides of the orifice. At 130 dB (figure 10(a)), the two contributions are nearly identical, while at 140 dB (figure 10(b)), moderate differences emerge, likely due to a thicker boundary layer forming on the upstream side.

Regarding the phase dependence, in the absence of grazing flow, the inflow and outflow dissipation profiles remain largely symmetric. For SPL up to 150 dB (figure 10(a–c)), the dissipation exhibits two dominant lobes, indicating that viscous dissipation mainly occurs during the inflow and outflow phases. At 160 dB, additional lobes appear, suggesting

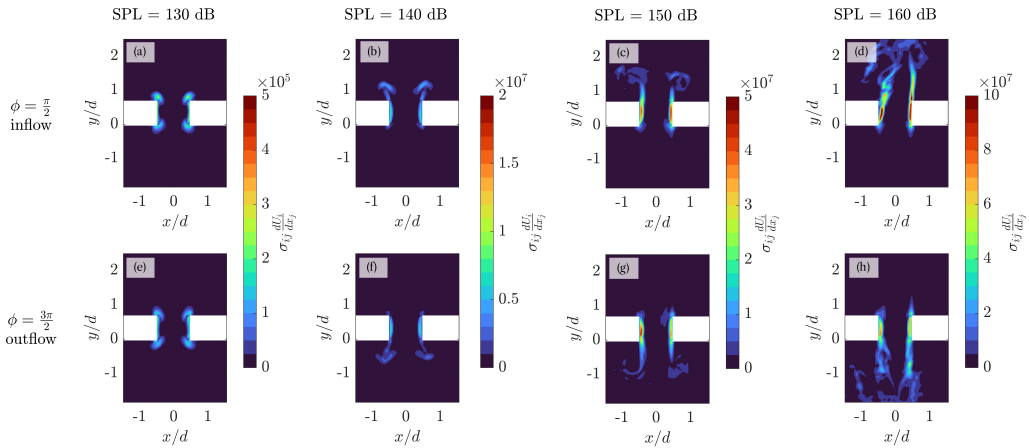


Figure 9. Contour of the turbulent stress tensor [Kg/(m-s²)] in the inflow and outflow phases when varying the SPL. $M = 0$ case, forcing frequency equal to 2200 Hz.

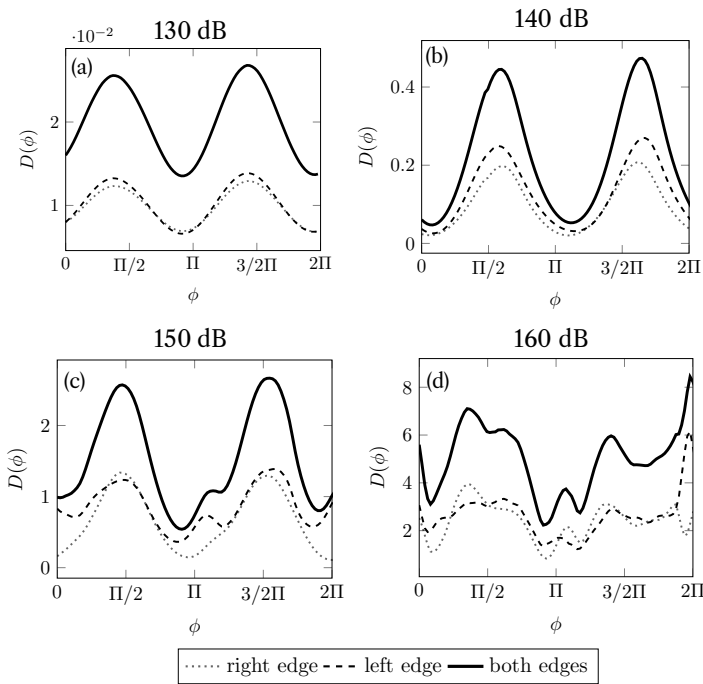


Figure 10. Phase averaged viscous dissipation rate as a function of the phase, $D(\phi)$ [W/(m-s)], in one cycle at different SPL, left and right orifice edge contribution reported separately, no flow case, forcing frequency equal to 2200 Hz.

that non-linear effects and higher harmonic components of the acoustic-induced velocity contribute to the dissipation.

When the grazing flow is introduced (figure 11), several significant changes arise. First, at low SPL, the contour levels are higher than in the no-flow case, showing an increase in viscous dissipation driven by the flow itself. This increase stems from the grazing flow

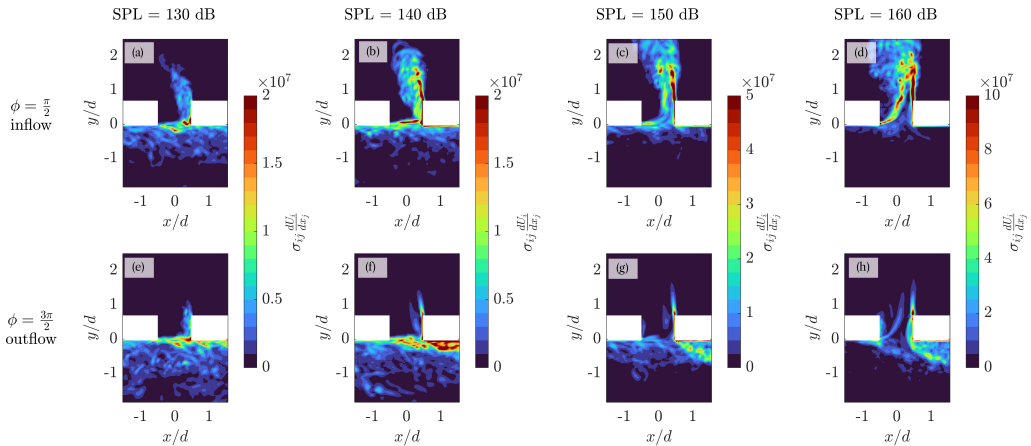


Figure 11. Contour of the turbulent stress tensor $[\text{Kg}/(\text{m}\cdot\text{s}^2)]$ in inflow and outflow phases when varying the SPL. $M = 0.3$ case, forcing frequency equal to 2200 Hz.

pushing the acoustic-induced flow preferentially towards the downstream (right) side of the orifice, as previously observed in the acoustic-induced velocity fields (figure 4).

A pronounced geometric asymmetry emerges: the dissipation is larger at the downstream side of the orifice, while the upstream side contributes negligibly. This is due to the quasi-steady vortex occupying the upstream half of the orifice, which blocks the flow through the orifice during the inflow and outflow phases. At higher SPL, a free-shear layer appears at the center of the orifice during the inflow phase (figure 11(c–d)). However, this contribution is not considered as wall viscous dissipation, as it corresponds to energy conversion into vorticity already accounted for in the vortex shedding dissipation.

Figure 12 quantifies separately the upstream and downstream wall contributions. The left side contribution remains negligible across SPL levels, except at 160 dB, where it becomes significant during the outflow phase (figure 12(d)). At this high SPL, the strong acoustic-induced outflow perturbs the quasi-steady vortex, allowing part of the flow to reach the upstream side and contributes to viscous dissipation.

Macroscopic differences in the viscous dissipation are evident in the phase evolution of the cumulative dissipation rate (left and right sides combined), summarised in figure 13 for the cases with and without grazing flow. At low SPL, the dissipation rate with grazing flow is an order of magnitude higher than in the no-flow case (as can be seen by looking at the scale in figure 10(a–b) with figure 12(a–b)). The outflow phase contribution remains negligible at low SPL (figure 13(b)) because the grazing flow inhibits the development of acoustic-induced flow during the outflow phase. As SPL increases, the outflow contribution becomes increasingly significant, and at 160 dB, a two-lobe pattern re-emerges, indicating that the high amplitude pressure fluctuations overcome the blocking effect of the grazing flow.

Finally, the temporal fluctuations of the dissipation rate during the inflow phase in the presence of flow (figure 13 (b)) are higher than in the no-flow case, because of the turbulence entering the orifice. In contrast, the outflow phase shows smoother variations, suggesting that most turbulent structures are dissipated after the inflow, and the flow grazing the walls in the outflow phase contains lower amplitude turbulent fluctuations—similar to the behavior observed in the no-flow case (figure 13 (a)).

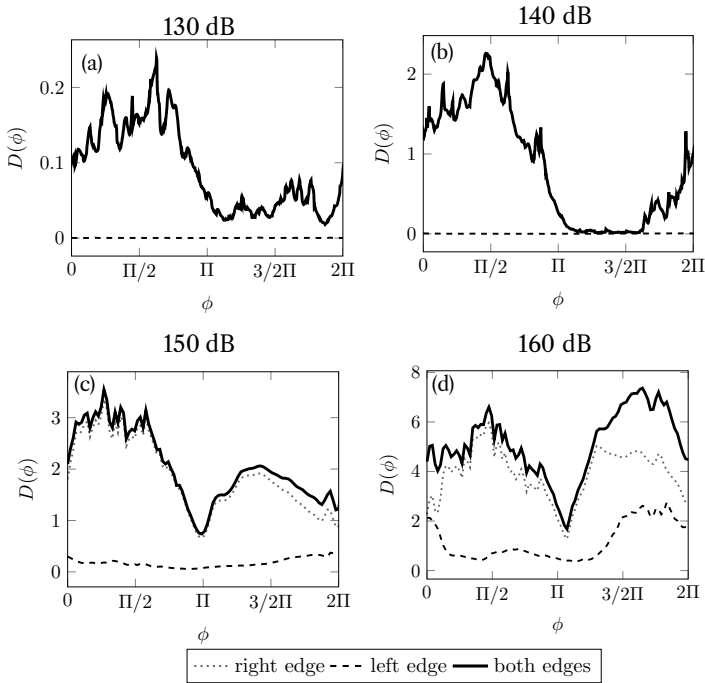


Figure 12. Phase averaged viscous dissipation rate a function of the phase, $D(\phi)$ [$\text{W}/(\text{m}\cdot\text{s})$], in one cycle at different SPL, left and right orifice edge contribution reported separately, $M=0.3$ condition, forcing frequency equal to 2200 Hz.

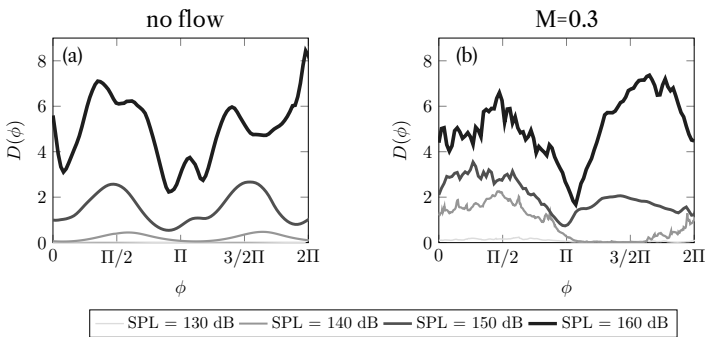


Figure 13. Phase averaged viscous dissipation rate, $D(\phi)$ [$\text{W}/(\text{m}\cdot\text{s})$] over one cycle at different SPL, contribution of both edges; (a) no flow condition, (b) $M=0.3$ condition, forcing frequency equal to 2200 Hz.

5.3. Energy budget

The net acoustic energy per unit time transferred to the vortical field by vortex shedding and the energy dissipated directly by wall viscosity, as functions of SPL, are shown in figure 14(a) for both the no-flow and grazing flow cases. All values are normalised by the corresponding impinging acoustic energy upstream of the orifice, E_i . The details of the calculation of E_i are reported in the Appendix B.

In the absence of grazing flow (red, solid squares), the net acoustic energy converted into vorticity increases with SPL: it remains negligible at 130 dB, becomes slightly larger at 140 dB, and rises more consistently at 150 dB before levelling off at 160 dB. Despite

differences in normalisation and the definition of E_i , these results are broadly consistent with earlier findings by Tam & Kurbatskii (2000). Conversely, the viscous dissipation contribution (red curve, empty triangles) dominates at low SPL but its relative importance decreases as SPL increases, becoming lower than the vortex shedding contribution at 160 dB.

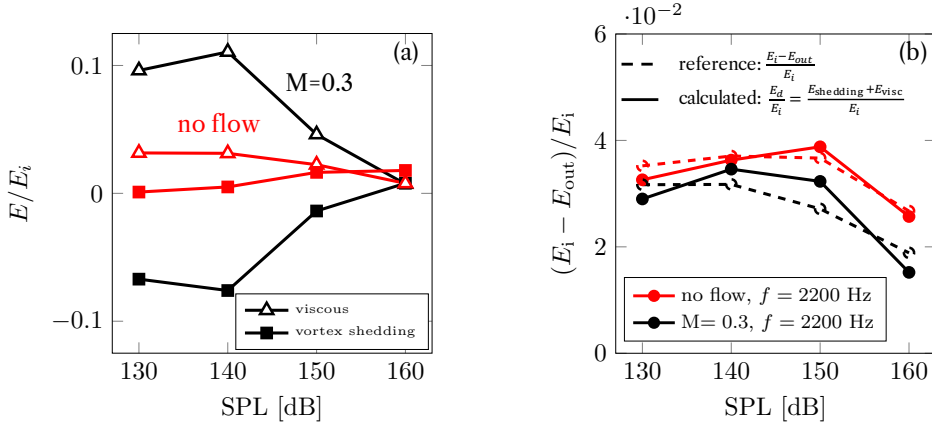


Figure 14. Energy budget as function of the SPL, (a) normalized energy per unit time dissipated by viscous and vortex shedding for the no flow case and for the $M=0.3$, (b) total budget, sum of the viscous and shedding contribution.

When the grazing flow is introduced (black line in figure 14(a)), the dissipation mechanisms change substantially. At low SPL (130 and 140 dB), the viscous dissipation becomes roughly three times higher than in the no-flow case. It increases slightly from 130 to 140 dB, highlighting that at low to moderately low SPL, grazing flow strongly modifies the dissipation process by increasing the viscous contribution. However, at higher SPL, the viscous dissipation in the grazing flow case approaches the level observed without flow, suggesting that the effect of high amplitude pressure fluctuations becomes predominant over flow-induced effects.

It is worth to note that the net vortex shedding contribution becomes negative up to 150 dB, indicating that, rather than dissipating acoustic energy, the vortex shedding process contributes to acoustic energy generation. This effect is driven by the outflow phase, where the acoustic-induced velocity exiting the orifice interacts with the grazing flow, producing vorticity that radiates downstream and add energy to the acoustic field. At 160 dB, the strong acoustic-induced velocity extends over a larger portion of the orifice diameter, while the shear layer is confined to a narrower region. The reduced obstruction allows the inflow phase to dominate over the outflow, resulting in a net positive dissipation. However, the magnitude of this positive contribution remains smaller compared to the no-flow case. Overall, these results suggest that, particularly at moderate SPL in the presence of grazing flow, vortex shedding can have a detrimental effect on the liner's noise absorption performance by reducing the net acoustic dissipation.

The total non-dimensional dissipated energy as a function of SPL for both configurations is presented in figure 14(b). The dashed line shows reference values computed by subtracting the energy integrated at a downstream plane, E_{out} , from the impinging energy E_i , while the solid line shows the sum of the viscous and vortex shedding contributions calculated separately. The good agreement between these curves indicates that the calculated dissipation contributions are physically consistent and capture the

dominant energy conversion mechanisms. Details on the calculation of the energy flow within the channel is reported in Appendix B.

For the no-flow case (red curves), the fraction of energy dissipated remains almost constant at about 4% up to 160 dB, where it suddenly drops. This decrease is likely related to the reduction of the viscous contribution at high SPL in the absence of flow. In the presence of grazing flow, however, the negative contribution from vortex shedding leads to a consistently lower overall dissipation at all SPL levels compared to the no-flow case, underscoring its adverse effect on the liner's acoustic performance.

6. Effect of the acoustic source frequency and acoustic propagation direction

6.1. Effect of the source frequency

In this section, we examine the influence of the acoustic excitation frequency while keeping the SPL fixed at 150 dB. The analysis is carried out both in the absence and in the presence of grazing flow.

In figure 15 (a,b), the acoustic-induced velocity profiles at the orifice centreline are reported for the inflow and outflow phases. The velocity is normalized using the theoretical acoustic-induced velocity at 2200 Hz, allowing a direct comparison across frequencies. Without grazing flow, the case at 1800 Hz exhibits the largest acoustic-induced velocity, as this frequency is the closest to the resonant frequency of the liner in quiescent conditions (approximately 1600 Hz). As the frequency increases beyond resonance, the amplitude of the velocity decreases accordingly.

When the grazing flow is introduced, the acoustic-induced velocity profiles at 1800 Hz and 2200 Hz become nearly indistinguishable, with only moderate differences near the downstream edge, which appears slightly more energetic at 2200 Hz. This shift can be attributed to a modification of the liner's effective resonant frequency caused by the grazing flow. The presence of a quasi-steady recirculating vortex at the upstream corner of the orifice reduces the effective flow area, thereby increasing the resonant frequency.

The rate of dissipation by vortex shedding in the absence of grazing flow is shown in figure 15 (c). As discussed in the previous sections, the dissipation remains positive in both inflow and outflow phases, with a slightly larger contribution during the inflow which might be due to the attenuation of acoustic waves as they exit the orifice. The largest dissipation occurs at the lowest frequency (1800 Hz), and it decreases as the forcing frequency moves away from resonance. When the grazing flow is present (figure 15 (d)), the dissipation by vortex shedding becomes positive during the inflow and negative during the outflow. The outflow contribution dominates thus resulting in a net negative shedding dissipation. The viscous dissipation rate is reported in figure 15 (e,f). The frequency dependence is more pronounced without grazing flow ($M=0$), whereas under grazing flow conditions the flow dynamics dominate, and the influence of frequency becomes weaker.

The normalized net acoustic energy per unit time dissipated by viscosity and transferred into vorticity as function of the frequency is reported in figure 16 (a). In the presence of grazing flow, the shedding contribution (black squares) remains negative but shows a local increase in magnitude around 2200 Hz. Nevertheless, a moderate increase in viscous dissipation is observed at 2200 Hz (figure 16 (a), black triangles), indicating that viscous losses remain sensitive to the resonant response of the system even in the presence of flow. In contrast, for the no-flow case (red squares), both dissipation mechanisms remain positive and decrease monotonically with increasing frequency.

Finally, figure 16 (b) summarizes the total normalized acoustic energy dissipation as a function of frequency. In the absence of flow, the maximum dissipation occurs near 1800 Hz, consistent with the liner's resonant frequency in quiescent conditions. In contrast,

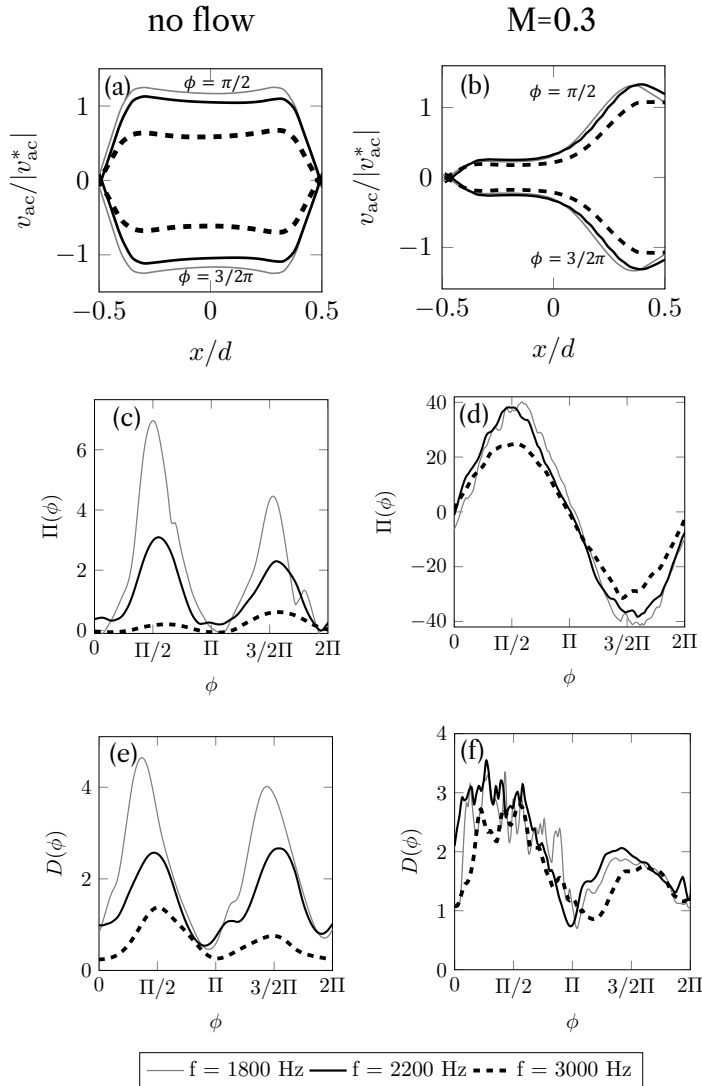


Figure 15. Effect of changing the source frequency on the acoustic-induced velocity profiles (a-b), rate of the acoustic energy dissipation by vortex shedding, $\Pi(\phi)$ [W/(m·s)] (c-d), viscous dissipation rate, $D(\phi)$ [W/(m·s)] in one cycle considering both orifice edges (e-f). The SPL is fixed at 150 dB, left column no flow condition, right column $M = 0.3$.

with grazing flow the peak shifts to 2200 Hz, confirming a resonance shift due to the modified effective porosity and flow–acoustic interaction at the orifice.

6.2. Effect of acoustic propagation direction

In this section, we examine the effect of reversing the acoustic wave propagation direction keeping fixed the SPL at 150 dB. Specifically, we consider the case where the acoustic wave propagates opposite to the grazing flow, this case is denoted as x^- .

In figure 17 (a), the acoustic-induced velocity profile at the orifice centreline is reported. Compared with the case where the acoustic wave is aligned with the grazing flow (x^+),

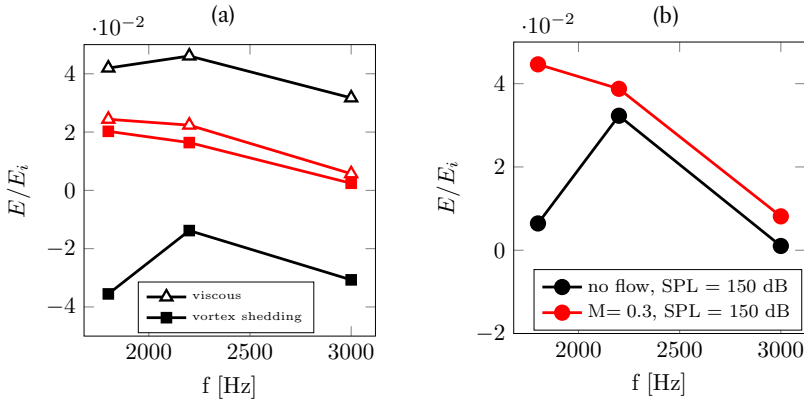


Figure 16. Energy budget as function of the frequency at SPL=150 dB, (a) normalized energy per unit time dissipated by viscous and vortex shedding for the no flow case and for the $M = 0.3$ case, (b) total budget, sum of the viscous and shedding contribution.

only moderate deviations are observed. The maximum velocity is slightly higher, and the boundary layer on the downstream wall of the orifice becomes thicker. This indicates a momentum enhancement through the orifice during both inflow and outflow phases, with a larger fraction concentrated in the downstream half of the orifice.

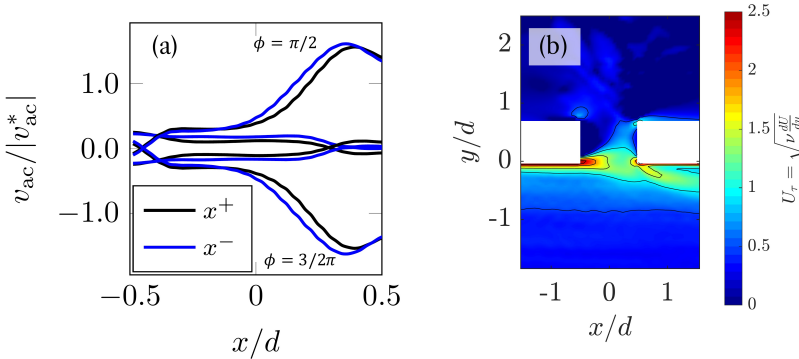


Figure 17. Acoustic wave propagating in the direction opposite to the flow, $M = 0.3$ case, forcing frequency equal to 2200 Hz, SPL = 150 dB; (a) acoustic-induced velocity profile comparison with the case with the wave propagating in the same direction of the flow, (b) contour of the friction velocity to represent the shear layer forming at the mouth of the orifice.

A possible explanation is that the acoustic waves generate an additional acoustic shear layer in the near-wall region which, for the x^- case, is oriented opposite to that induced by the grazing flow. The interaction between these counter-oriented shear layers modifies the effective shear velocity, as shown in figure 17(b), which can be directly compared with the reference x^+ case reported in figure 5(c). As a result, both the shear region above the orifice and the quasi-steady vortex are reduced in extent, yielding a broader distribution of the acoustic-induced velocity within the orifice during both phases.

In figure 18, the dissipation by vortex shedding and viscous effects is summarized. Subfigures (a) and (c) report the contours of the rate of acoustic energy converted into vorticity during the inflow and outflow phases, respectively, while subfigures (b) and (d)

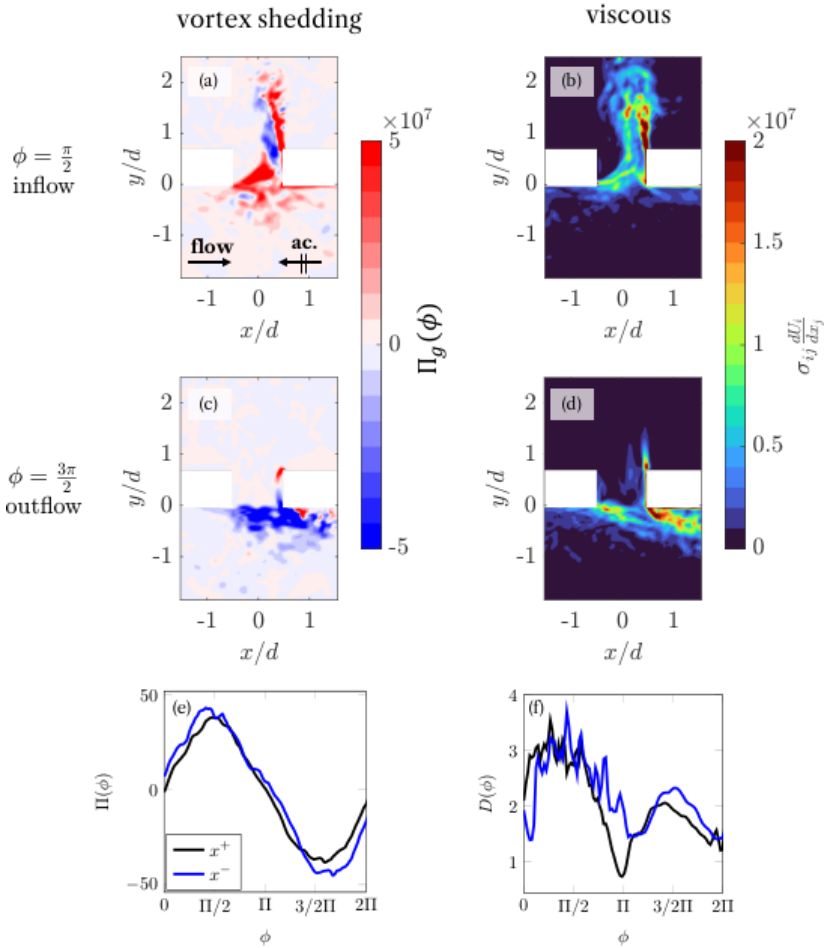


Figure 18. Acoustic wave propagating in the direction opposite to the flow, x^- , $M = 0.3$ condition, forcing frequency equal to 2200 Hz, SPL = 150 dB. Contour of the power density transferred from the acoustic to the vortical field, Π_g [$\text{Kg}/(\text{m}\cdot\text{s}^2)$] and contour of the stress tensor [$\text{Kg}/(\text{m}\cdot\text{s}^2)$] for the inflow (a-b) and outflow phase (c-d), rate of the acoustic energy dissipation by vortex shedding, $\Pi(\phi)$ [$\text{W}/(\text{m}\cdot\text{s})$], and by viscous effects $D(\phi)$ [$\text{W}/(\text{m}\cdot\text{s})$], comparison with the case with wave propagating in the same flow direction, x^+ , (e-f).

show the corresponding viscous dissipation. The quantitative comparison with the x^+ case is provided in figure 18 (e,f).

Looking at the dissipation by vortex shedding, both inflow and outflow phases contribute more in the x^- case than in the x^+ configuration. This behaviour is directly connected to the reduced obstruction of the shear region above the orifice and the momentum enhancement across the orifice. However, the enhanced magnitude in the inflow and outflow largely offset one another, resulting in a limited net effect.

In contrast, viscous dissipation exhibits a consistently larger contribution in the x^- case, in agreement with the observed thickening of the boundary layer along the orifice walls. The viscous contribution increases markedly during the inflow phase, where the dissipation pattern becomes more irregular than in the x^+ case. This behaviour might indicate that the turbulent structures entering the orifice originate from the interaction between the two counter-oriented shear layers, one produced by the acoustic wave and the other by the grazing flow. During the outflow phase, the higher exit velocity enhances viscous

dissipation near the downstream lip. This enhancement can be attributed to the reduction of the shear region above the orifice: with less obstruction from the grazing flow, the outflow jet develops more freely and interacts more strongly with the orifice walls. As a result, the total viscous dissipation becomes higher than in the x^+ case.

These observations underline that modifying the shear layer, whether by reversing the acoustic wave direction or by altering the impinging velocity profile, leads to significant changes in the dissipation mechanisms. This suggests that, in more realistic liners composed of multiple cavities, the streamwise development of the grazing boundary layer and its interaction with successive orifices could play a crucial role in affecting the local dissipation characteristics.

7. Concluding remarks

The present study investigates the dissipation mechanisms of an acoustic liner subjected to grazing turbulent flow through high-fidelity lattice-Boltzmann very-large-eddy simulations. A two-dimensional domain centred on a single orifice of a single cavity liner was analysed to isolate the physical mechanisms responsible for acoustic energy dissipation, independently from flow development effects. The analysis covered a range of SPLs from 130 to 160 dB and frequencies between 1800 and 3000 Hz. The main findings are summarised below, addressing the key research questions posed in the introduction.

The presence of grazing turbulent flow alters the flow topology inside the orifice and, through that modification, the mechanisms of acoustic energy dissipation. In the no-flow configuration, the acoustically induced velocity field is almost symmetric across the orifice and both inflow and outflow phases contribute positively to the conversion of acoustic energy into vortical motion and to viscous losses. By contrast, grazing flow generates a near-wall shear layer above the orifice and produces a quasi-steady recirculating vortex occupying the upstream half of the orifice. This vortex reduces the effective open area of the orifice and confines the acoustic-induced motion to the downstream half. The altered topology concentrates the regions of strong vorticity production and wall shear at the downstream half of the orifice and modifies the spatial distribution of the dissipation rate.

In the absence of grazing flow, both the inflow and outflow phases contribute positively to the dissipation of acoustic energy, with vortex shedding dominating at high SPL and viscous effects prevailing in the linear regime. The topological change introduced by the grazing flow has two direct and measurable consequences for the dissipation budget. First, the contribution of vortex shedding becomes strongly phase dependent: the inflow phase shows enhanced conversion of acoustic energy into vorticity because turbulent structures from the grazing flow are entrained into the orifice, whereas the outflow phase acts as an acoustic source. During the outflow, the acoustic-induced velocity interacts with the grazing flow and produces vortical structures (akin to those produced by a jet in cross-flow) that radiate acoustic energy; consequently the net shedding contribution (integrated over a full cycle) reduces and may become negative at low–moderate SPL. Second, viscous dissipation at the orifice walls increases where the grazing flow pushes fluid toward the downstream lip: at low SPL this wall contribution is substantially larger than in the no-flow case but limited to the inflow phase. At sufficiently high SPL the viscous term approaches values comparable with the quiescent configuration. At the highest SPLs considered, in fact, inflow and outflow contributions to the viscous dissipation become more symmetric and the overall asymmetries between upstream and downstream orifice lip and inflow and outflow phases are attenuated, approaching the condition obtained in absence of flow. However, the reduced net contribution from shedding in the presence of grazing flow

remains a principal factor lowering the liner's net energy absorption compared with the no-flow case.

In sum, the grazing flow modifies where and in which phase energy is exchanged between acoustics and fluid motion. At low SPL, viscous dissipation dominates during the inflow phase and it is concentrated near the downstream lip of the orifice, whereas the outflow phase provides a negligible contribution to the viscous dissipation. The dominant mechanism by which the grazing flow reduces the liner's net absorption is the transformation of the outflow phase from a dissipative to a generative mechanism of acoustic energy via vortex shedding, only partially compensated by the increased viscous losses at the downstream wall.

Additional analyses demonstrated that the excitation frequency and the direction of acoustic wave propagation also influence the liner response. At constant SPL, the dissipation reaches its maximum near the resonant frequency of the system. In the absence of flow, this occurs around 1800 Hz, while in the presence of grazing flow the resonant frequency shifts to approximately 2200 Hz owing to a reduced effective porosity induced by the quasi-steady vortex. Similarly, when the acoustic wave propagates opposite to the grazing flow, the shear layer above the orifice is weakened, promoting deeper acoustic penetration into the cavity and slightly enhancing overall dissipation.

Finally, the current results show that the grazing flow not only modifies the impedance but alters the balance between viscous and vortical dissipation mechanisms. The most important take away message is that the outflow phase, in particular, is detrimental to the noise absorption capability of an acoustic liner. Future work should focus on the streamwise evolution of the dissipation along multi-orifice liners, where the grazing flow development and the mutual interaction between cavities are expected to further influence the local acoustic dissipation. Ongoing work is dedicated to assess, from a dissipation standpoint, how variations in orifice geometry, such as the edge shape, modify the balance between viscous and vortex-shedding mechanisms. Such insights may guide the design of advanced liners, including meta-structured orifices or flow-control strategies that mitigate outflow-induced acoustic generation.

Declaration of Interests

The authors report no conflict of interest.

Funding Sources

The work of F. Scarano, A. Paduano and F. Avallone is funded by the European Union (ERC, LINING, 101075903). Views and opinions expressed are however those of the author(s) only and do not necessarily reflect those of the European Union or the European Research Council. Neither the European Union nor the granting authority can be held responsible for them.

Appendix A. Grid convergence study, validation of the baseline cases with reference experiments and impedance results in presence and in absence of grazing flow

The incoming turbulent boundary layer for the case with grazing flow is presented in Figure 19. The Mach number profile for the three grid resolutions is plotted in Figure 19(a) and compared against the experimental data; it shows that only minor variations are present between the two finest grids. Since the case with maximum grid resolution of 40 voxels/ d shows a converging trend and a good agreement with the experiments, for this grid resolution the streamwise variance $\langle u'^2 \rangle$ is presented in wall-units in Figure 19(c). The profile of the

streamwise variance is compared against numerical and experimental data from the literature (Zhang & Bodony 2016b; De Graaff & Eaton 2000).

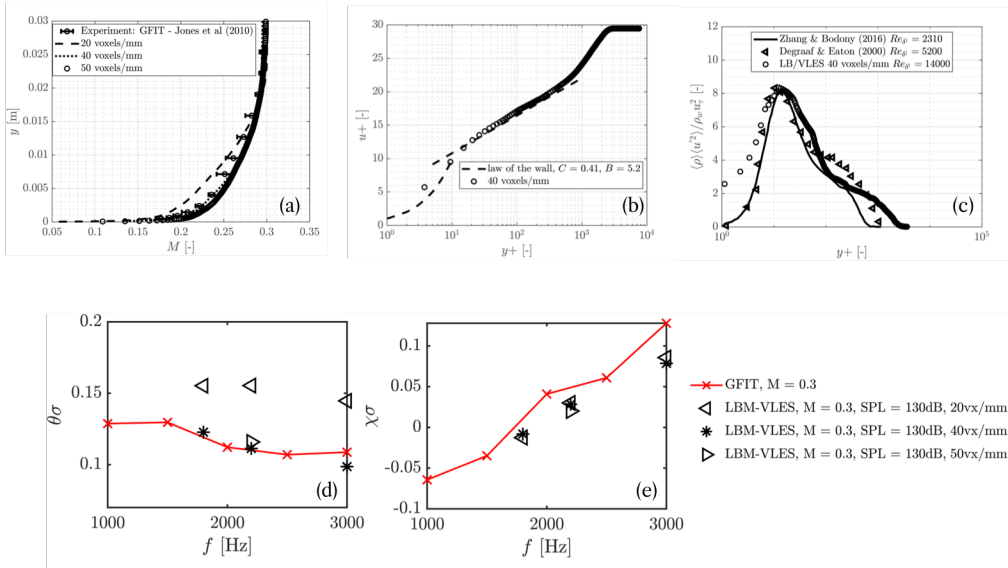


Figure 19. (a) Streamwise Mach number profile of the incoming turbulent grazing flow for three grid resolutions compared with the experiments; (b) velocity profiles in wall units and comparison with log-law and experimental data; (c) normalized streamwise variance compared with the literature; (d) acoustic resistance and (e) reactance for the three grid resolutions compared with experimental results at $M = 0$.

The grid convergence is verified also for the impedance for the simulations without flow at the three frequencies at a fixed SPL = 130 dB. The computed impedance is compared with experimental data obtained at the GFIT facility (GIT-95M test section) (Jones *et al.* 2004), where impedance was extracted using a two-dimensional finite element method (2D-FEM). In the present numerical framework, the acoustic impedance is evaluated using the in-situ technique, originally introduced by Dean (1974b), which relies on pressure measurements acquired at two distinct locations within the liner: at the face sheet and at the backplate of the cavity. This method, often referred to as the two-microphone approach, provides a local estimation of impedance and is applicable under the assumptions that: (i) the acoustic wavelength is significantly larger than the cavity width; (ii) the cavity behaves as a locally reactive element due to sufficiently thick side walls; and (iii) acoustic waves entering the cavity are fully reflected at the backplate. This method is particularly suited to the current study, as only a single cavity is simulated.

Time-resolved pressure signals are sampled at discrete locations to reconstruct the transfer function between face sheet and backplate. Specifically, pressure at the face sheet is recorded every 30° along a circular contour of radius $1d$ centred on each orifice, while the backplate pressure is sampled at the orifice centres. The resulting transfer functions are then averaged across all spatial locations to improve robustness. The impedance values finally averaged out of the 7 orifices.

Following the formulation in Dean (1974a), Manjunath *et al.* (2018) and Avallone *et al.* (2019), the normalized acoustic impedance Z_f is obtained via:

$$Z_f = \frac{Z}{Z_0} = -i\tilde{H}_{fb} \frac{1}{\sin(k\zeta)}, \quad (\text{A } 1)$$

where Z_0 is the characteristic impedance of air, $\tilde{H}_{fb} = \tilde{p}_f / \tilde{p}_b$ is the complex pressure transfer function between face sheet and backplate, ζ is the cavity depth, and $k = \omega/c_0$ is the acoustic wavenumber, with ω the angular frequency and c_0 the speed of sound.

The two components of the impedance, the resistance, θ , and the reactance, χ , are shown in figure 19(c-d); they are both scaled with the porosity, σ , to allow comparison with the reference experiments in absence of grazing flow. As for the turbulent boundary layer, the case with resolution equal to 40 voxels/ d shows converging results and good agreement with the experimental results.

In figure figure 20 the impedance for the cases with ($M=0.3$) and without ($M=0$) grazing turbulent flow for varying SPL of the grazing acoustic wave at a frequency of 2200 Hz are compared. The two components of the acoustic impedance, resistance and reactance, averaged out of the 7 orifices and scaled by the liner porosity σ , are plotted.

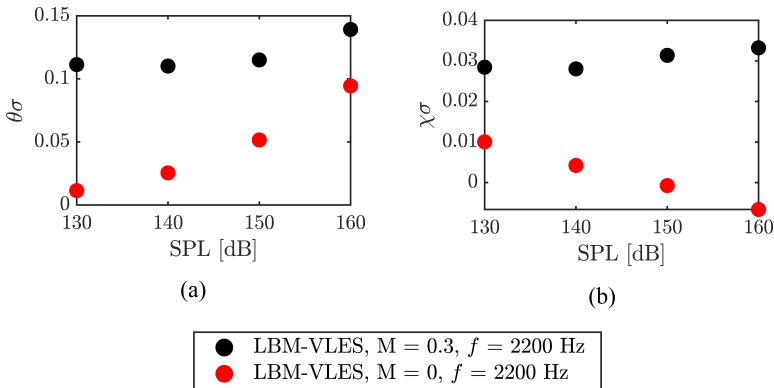


Figure 20. (left) Resistance θ and (right) reactance χ components of impedance scaled with the liner porosity σ . The frequency of the acoustic wave is 2200 Hz, while the amplitude varies between 130 and 160 dB.

The results show that, with increasing SPL, the resistance θ grows more significantly in the absence of flow compared to the case with grazing turbulent flow. Specifically, while θ exhibits an exponential increase without flow, it remains nearly constant up to 150 dB in the presence of flow, only starting to increase at higher SPL. Additionally, it is observed that, in the presence of grazing flow, the amplitude of θ is comparable to the maximum value attained in the no-flow case. The grazing flow also affects the reactance, χ : for $M = 0$, χ decreases with increasing SPL, whereas for $M = 0.3$, it slightly increases with SPL. These results clearly demonstrate that the acoustic impedance is significantly altered by the presence of a grazing turbulent flow. This behavior may be related to modifications in the acoustic-induced flow topology and the associated dissipation mechanisms.

Appendix B. Evaluation of the impinging acoustic energy

The acoustic energy used to normalize the dissipation terms in figure 14 is computed by integrating the fluctuating pressure field along the entire channel height, as illustrated in figure 21. This differs from the definition adopted by Tam & Kurbatskii (2000), where the orifice surface was used as the reference dimension.

The procedure is grounded in the acoustic energy conservation law (Rienstra & Hirschberg 2004), which states that for a time-periodic acoustic field the mean acoustic energy flux through a control surface equals the dissipation within the enclosed volume. In the present case, the dissipation comprises two distinct contributions: viscous losses and the conversion of acoustic energy into vortical motion. This framework allows a direct comparison between the total dissipated energy (obtained by summing the individual contributions) and the net flux balance between E_i and E_{out} , providing an internal validation of the energy budget.

With this definition, the impinging energy E_i upstream of the orifice and the outgoing energy E_{out} downstream can be consistently compared. Shifting the evaluation planes within two orifice diameters upstream or downstream does not affect the results, confirming the robustness of the method.

In practice, the acoustic flux requires the distribution of the acoustic energy upstream and downstream of the orifice. Since the field analysed is two-dimensional, the surface integral reduces to an integration along the wall-normal direction, while the volume integral corresponds to the two-dimensional control region.

Representative wall-normal profiles of the acoustic energy (normalized with the reference pressure and reported in dB) are shown in figure 21 for SPL = 130 and 150 dB for the sake of conciseness. In the absence of grazing flow (subfigures (a,c)), the distribution resembles an acoustic boundary layer: energy peaks at the channel centreline and decreases towards the wall. Downstream of the orifice, the profiles exhibit the expected attenuation due to dissipation.

When a grazing flow is introduced at 130 dB (subfigure (b)), the profiles are markedly altered. The acoustic energy increases towards the wall, reflecting the contribution of turbulence-induced pressure fluctuations in the boundary layer. Downstream of the orifice, the energy decreases in the channel core but slightly increases near the wall due to the interaction of the shear layer with the orifice jet.

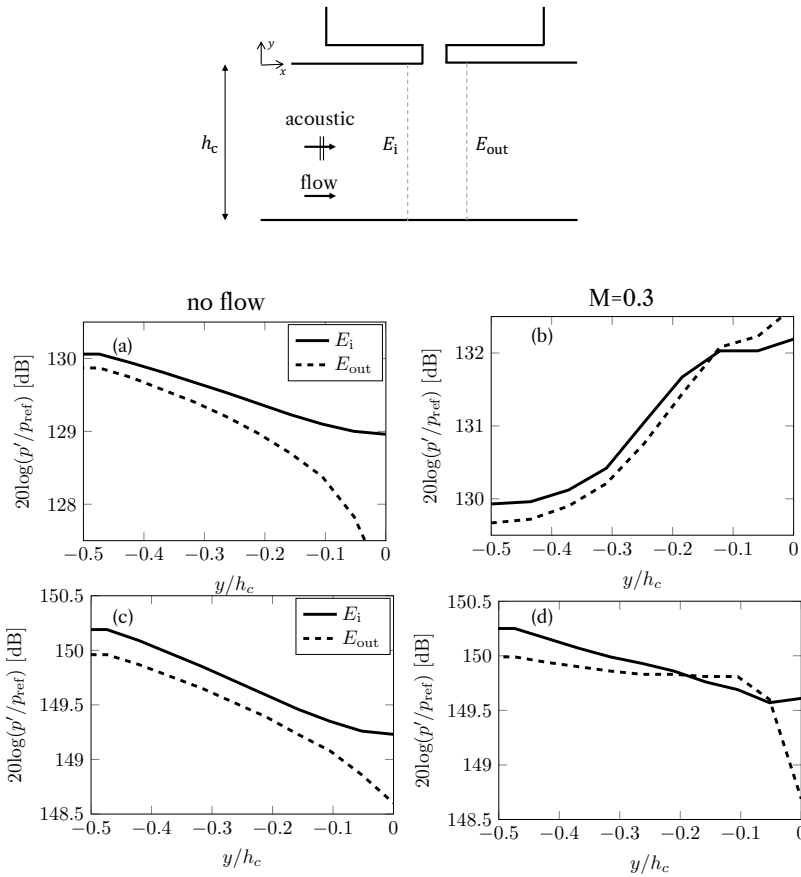


Figure 21. Methodology for evaluating the impinging acoustic energy E_i [W/m] and downstream energy E_{out} along the channel height. Energy distributions in [dB] are reported for (a,b) SPL = 130 dB without and with grazing flow, and (c,d) SPL = 150 dB.

At 150 dB with grazing flow (subfigure (d)), the profiles more closely resemble the no-flow case: the acoustic source dominates over the background turbulence, yielding a higher acoustic-to-aerodynamic fluctuation ratio, in agreement with Scarano *et al.* (2025). Interestingly, downstream of the orifice the energy distribution exhibits a local maximum not at the wall but around $y/h_c \approx -0.1$, suggesting that the stronger jetting effect at this SPL penetrates deeper into the grazing flow and locally amplifies the pressure fluctuations.

REFERENCES

- AVALLONE, F., MANJUNATH, P., RAGNI, D. & CASALINO, D. 2019 Lattice-Boltzmann Very Large Eddy Simulation of a Multi-Orifice Acoustic Liner with Turbulent Grazing Flow. In *25th AIAA/CEAS Aeroacoustics Conference*, pp. 2019–2542. Reston, Virginia: American Institute of Aeronautics and Astronautics.
- BAUMEISTER, K.J. & RICE, E.J. 1975a Visual study of the effect of grazing flow on the oscillatory flow in a resonator orifice. *Tech. Rep.*. NASA Lewis Research Center, Cleveland, OH, United States.
- BAUMEISTER, KENNETH J. & RICE, EDWARD J 1975b NASA TM X-3288 2. Government Accession No. 4. Title and Subtitle visual study of the effect of grazing flow on the oscillatory flow in a resonator orifice .
- BONOMO, LUCAS A, QUINTINO, NICOLAS T, CORDIOLI, JULIO A, AVALLONE, FRANCESCO, JONES, MICHAEL G, HOWERTON, BRIAN M & NARK, DOUGLAS M 2023 A Comparison of Impedance Eduction Test Rigs with Different Flow Profiles. *Tech. Rep.*.
- CAMELIER, JEAN & KARAMCHETI, KRISHNAMURTY 1976 An experimental study of the structure and acoustic field of a jet in a cross stream. *Tech. Rep.* NASA CR-162464. NASA, Washington, D.C., nASA Contractor Report 162464.
- CASALINO, D., HAZIR, A.G. & MANN, A. 2017 Turbofan Broadband Noise Prediction Using the Lattice Boltzmann Method. *AIAA Journal* **56** (2), 1–20.
- CASALINO, D., HAZIR, A. & MANN, A. 2018 Turbofan broadband noise prediction using the lattice boltzmann method. *AIAA Journal* **56** (2).
- CHEN, H., GOPALAKRISHNAN, P. & ZHANG, R. 2014 Recovery of Galilean invariance in thermal lattice Boltzmann models for arbitrary Prandtl number. *International Journal of Modern Physics C* **25** (10), 1450046.
- CHEN, H, ORSZAG, S.A., STAROSELSKY, I. & SUCCI, S. 2004 Expanded analogy between Boltzmann kinetic theory of fluids and turbulence. *Journal of Fluid Mechanics* **519**, 301–314.
- CHEN, S. & DOOLEN, G.D. 1998 Lattice Boltzmann method for fluid flows. *Annual Review of Fluid Mechanics* **30** (1), 329–364.
- DE GRAAFF, D.B. & EATON, J.K. 2000 Reynolds-number scaling of the flat-plate turbulent boundary layer. *Journal of Fluid Mechanics* **422**, 319–346.
- DEAN, P.D. 1974a An in situ method of wall acoustic impedance measurement in flow ducts. *Journal of Sound and Vibration* **34** (1), 97–IN6.
- DEAN, P D 1974b An in situ method of wall acoustic impedance measurement in flow ducts. *Tech. Rep.* 1.
- HAZIR, A.G. & CASALINO, D. 2017 Effect of Temperature Variations on the Acoustic Properties of Engine Liners. In *23rd AIAA/CEAS Aeroacoustics Conference*, pp. 2017–3874.
- HOWE, M.S. 1980 The dissipation of sound at an edge. *Journal of Sound and Vibration* **70** (3), 407–411.
- HOWE, M. S. 1975 Contributions to the theory of aerodynamic sound, with application to excess jet noise and the theory of the flute. *Journal of Fluid Mechanics* **71** (4), 625–673.
- HOWE, M. S. 1984 On the Absorption of Sound by Turbulence and Other Hydrodynamic Flows. *IMA Journal of Applied Mathematics* **32** (1-3), 187–209.
- HUGHES, CHRIS 2011 The Promise and Challenges of Ultra High Bypass Ratio Engine Technology and Integration. *AIAA Aero Sciences Meeting* pp. 0–11.
- JONES, MICHAEL, WATSON, WILLIE & NARK, DOUGLAS 2010 Effects of Flow Profile on Educued Acoustic Liner Impedance. In *16th AIAA/CEAS Aeroacoustics Conference*, pp. 2010–3763. Reston, Virigina: American Institute of Aeronautics and Astronautics.
- JONES, M., WATSON, W., PARROTT, T.L. & SMITH, C. 2004 Design and Evaluation of Modifications to the NASA Langley Flow Impedance Tube. In *10th AIAA/CEAS Aeroacoustics Conference*, pp. 2004–2837. Reston, Virigina: American Institute of Aeronautics and Astronautics.
- LÉON, OLIVIER, MÉRY, FABIEN, PIOT, ESTELLE & CONTE, CLAUDIA 2019a Near-wall aerodynamic response of an acoustic liner to harmonic excitation with grazing flow. *Experiments in Fluids* **60** (9), 144.
- LÉON, OLIVIER, MÉRY, FABIEN, PIOT, ESTELLE & CONTE, CLAUDIA 2019b Near-wall aerodynamic response of an acoustic liner to harmonic excitation with grazing flow. *Experiments in Fluids* **60** (9).
- MALLAT, STEPHANE G 1989 A Theory for Multiresolution Signal Decomposition: The Wavelet Representation. *Tech. Rep.* 7.
- MANJUNATH, P., AVALLONE, F., CASALINO, D., RAGNI, D. & SNELLEN, M. 2018 Characterization of Liners using a Lattice-Boltzmann Solver. In *2018 AIAA/CEAS Aeroacoustics Conference*, pp. 2018–4192.
- MANN, A., PEROT, F., KIM, M.-S. & CASALINO, D. 2013 Characterization of Acoustic Liners Absorption using a Lattice-Boltzmann Method. In *19th AIAA/CEAS Aeroacoustics Conference*, pp. 2013–2271.
- MELLING, T H 1973 The acoustic impedance of perforates at medium and high sound pressure levels. *Tech. Rep.* 1.
- MORSE, P.M. & INGARD, K.U. 1968 *Theoretical Acoustics*. Princeton University Press.
- MOTSINGER, R.E. & KRAFT, R.E. 1991a Design and performance of duct acoustic treatment. In *Aeroacoustics of*

- Flight Vehicles: Theory and Practice. Volume 2: Noise Control* (ed. H.H. Hubbard), chap. 14, pp. 165–206. NASA.
- MOTSINGER, R E & KRAFT, R E 1991*b* 4 Design and Performance of Duct Acoustic Treatment. *Tech. Rep.*
- PADUANO, ANGELO, SCARANO, FRANCESCO, CORDIOLI, JULIO, CASALINO, DAMIANO & AVALLONE, FRANCESCO 2025 On the impact of the turbulent grazing flow development on the acoustic response of an acoustic liner. *arXiv preprint arXiv:2507.22714*.
- PANTON, RONALD L. & MILLER, JOHN M. 1975 Resonant frequencies of cylindrical helmholtz resonators. *The Journal of the Acoustical Society of America* **57** (6), 1533–1535, arXiv: https://pubs.aip.org/asa/jasa/article-pdf/57/6/1533/11595089/1533_1_online.pdf.
- RIENSTRA, S.W. & HIRSCHBERG, A. 2004 *An introduction to acoustics*. Technische Universiteit Eindhoven, extended and revised edition of IWDE 92-06.
- RONCEN, RÉMI 2025 Revisiting nonlinear impedance in acoustic liners. *Journal of Sound and Vibration* **608**, 119058.
- SCARANO, FRANCESCO, LYU, BENSUAI, PADUANO, ANGELO & AVALLONE, FRANCESCO 2025 Filtering acoustic from hydrodynamic velocity using modal decomposition methods on an acoustic liner under grazing turbulent flow. *Journal of Sound and Vibration* p. 119568.
- SCHMIDT, OLIVER T. & COLONIUS, TIM 2020 Guide to Spectral Proper Orthogonal Decomposition. *AIAA Journal* **58** (3), 1023–1033.
- SCHODER, STEFAN, ROPPERT, KLAUS & KALTENBACHER, MANFRED 2020 Postprocessing of Direct Aeroacoustic Simulations Using Helmholtz Decomposition. *AIAA Journal* **58** (7), 3019–3027.
- SHAHZAD, HARI, HICKEL, STEFAN & MODESTI, DAVIDE 2023 Direct Numerical Simulation of a Turbulent Boundary Layer over Acoustic Liners. American Institute of Aeronautics and Astronautics (AIAA).
- SHAHZAD, HARI, HICKEL, STEFAN & MODESTI, DAVIDE 2025 Direct numerical simulation of a turbulent boundary layer over acoustic liners. *AIAA Journal* **63** (11), 4650–4661, arXiv: <https://doi.org/10.2514/1.J065204>.
- SHAN, X., YUAN, X.-F. & CHEN, H. 2006 Kinetic theory representation of hydrodynamics: a way beyond the Navier–Stokes equation. *Journal of Fluid Mechanics* **550**, 413–441.
- SHUR, M., STRELETS, M., TRAVIN, A., SUZUKI, T. & SPALART, P. 2021 Unsteady Simulations of Sound Propagation in Turbulent Flow Inside a Lined Duct. *AIAA Journal* pp. 1–17.
- STIMPERT, D. L. & FOGG, R. G. 1973 Effect of crossflow velocity on the generation of lift fan jet noise in vtol aircraft. *Tech. Rep.* NASA CR-114571. NASA, Washington, D.C., nASA Contractor Report 114571.
- TABATA, RYOYA, MATSUDA, REI, KOIWAYA, TOSHIKI, IWAGAMI, SHO, MIDORIKAWA, HIROKO, KOBAYASHI, TAIZO & TAKAHASHI, KI`NYA 2021 Three-dimensional numerical analysis of acoustic energy absorption and generation in an air-jet instrument based on Howe’s energy corollary. *The Journal of the Acoustical Society of America* **149** (6), 4000–4012.
- TAM, C.K.W., JU, H., JONES, M.G., WATSON, W.R. & PARROTT, T.L. 2009 A computational and experimental study of resonators in three dimensions. *Journal of Sound and Vibration* **329**, 5164–5193.
- TAM, CHRISTOPHER K. W. & KURBATSKII, KONSTANTIN A. 2000 Microfluid Dynamics and Acoustics of Resonant Liners. *AIAA Journal* **38** (8), 1331–1339.
- TANG, YUCHAO, WANG, PENG & LIU, YINGZHENG 2024 PIV measurements of coherent vortices and turbulence production inside acoustic liner cavity with offset slit. *Experimental Thermal and Fluid Science* **154**, 111157.
- TEIXEIRA, C.M. 1998 Incorporating Turbulence Models into the Lattice-Boltzmann Method. *International Journal of Modern Physics C* **09** (08), 1159–1175.
- TOWNE, AARON, SCHMIDT, OLIVER T. & COLONIUS, TIM 2018 Spectral proper orthogonal decomposition and its relationship to dynamic mode decomposition and resolvent analysis. *Journal of Fluid Mechanics* **847**, 821–867.
- UNNIKRISHNAN, S. & GAITONDE, DATTA V. 2020 A pressure decomposition framework for aeroacoustic analysis of turbulent jets. *European Journal of Mechanics - B/Fluids* **81**, 41–61.
- WINKLER, J., MENDOZA, J.M., REIMANN, C.A., HOMMA, K. & ALONSO, J.S. 2021 High fidelity modeling tools for engine liner design and screening of advanced concepts:. *International Journal of Aeroacoustics* **0** (0), 1–31.
- YAKHOT, V., ORSZAG, S.A., THANGAM, S., GATSKI, T.B. & SPEZIALE, C.G. 1992 Development of turbulence models for shear flows by a double expansion technique. *Physics of Fluids A* **4** (7), 1510–1520.
- YOSHIKAWA, SHIGERU, TASHIRO, HIROMI & SAKAMOTO, YUMIKO 2012 Experimental examination of vortex-sound generation in an organ pipe: A proposal of jet vortex-layer formation model. *Journal of Sound and Vibration* **331** (11), 2558–2577.
- ZHANG, Q. & BODONY, D.J. 2012*a* Numerical investigation and modelling of acoustically excited flow through a circular orifice backed by a hexagonal cavity. *Journal of Fluid Mechanics* **693**, 367–401.
- ZHANG, Q. & BODONY, D.J. 2016*a* Direct numerical investigation of acoustic liners with single and multiple

- orifices grazed by a Mach 0.5 boundary layer. In *46th AIAA Fluid Dynamics Conference*. Reston, Virginia: American Institute of Aeronautics and Astronautics.
- ZHANG, QI & BODONY, DANIEL J. 2012*b* Numerical investigation and modelling of acoustically excited flow through a circular orifice backed by a hexagonal cavity. *Journal of Fluid Mechanics* **693**, 367–401.
- ZHANG, QI & BODONY, DANIEL J. 2016*b* Numerical investigation of a honeycomb liner grazed by laminar and turbulent boundary layers. *Journal of Fluid Mechanics* **792**, 936–980.
- ZHANG, R., SHAN, X. & CHEN, H. 2006 Efficient kinetic method for fluid simulation beyond the Navier-Stokes equation. *Physical Review E - Statistical, Nonlinear, and Soft Matter Physics* **74** (4), 046703.